

The $z=2.72$ galaxy cB58: a gravitational fold arc lensed by the cluster MS 1512+36 [★]

Stella Seitz,¹ R.P. Saglia,² Ralf Bender,² Ulrich Hopp,² Paola Belloni²
and Bodo Ziegler²

¹*Max-Planck-Institut für Astrophysik, P.O. Box 1523, D-85740 Garching, Germany*

²*Universitätssternwarte München, Scheinerstr. 1, D-81679 München, Germany*

4 April 2018

ABSTRACT

Using HST WFPC2 V- and R-band data of the $z = 0.37$ cluster MS1512+36 we show that the $z = 2.72$ ‘protogalaxy’ cB58 is not extraordinarily luminous intrinsically but lensed into a gravitational fold arc by the cluster. The arc has a surface brightness weighted axis ratio of 1 : 7, is marginally resolved in width and about 3'' long. Its counterimage was identified and found to be very compact ($r_{1/2} = 2.4 - 4.0 h_{50}^{-1}$ kpc in a $q_0 = 0.05$ cosmology). In addition, we found three further multiple image systems, one with five and two with three images each. The positions of the multiple images can be explained by modelling the light deflection caused by the cluster and the cD-galaxy with elliptical isothermal potentials. The major axis of the cluster potential approximately agrees with that of the cD-light and that of the X-ray isophotes. Since the multiple images are within $\approx 8''$ around the cD galaxy, a cluster core radius - cluster velocity dispersion degeneracy arises. Interpreting the observations conservatively, the cluster velocity dispersion and the core radius are limited to 540 – 670 km/s and 5'' – 11'', respectively, and the brightness of the unlensed counterimage of cB58 is about 23.9 ± 0.3 (R-band), corresponding to a magnification and extinction corrected restframe-B band absolute magnitude of -24.75 ± 0.7 mag. The redshifts of the sources of the remaining three multiple image systems are predicted to be similar to that of cB58 while a strict upper limit of 4 is set as they are visible in B-band ground based data. That part of the source of cB58 which is mapped into the arc is reconstructed and its magnification is found to be $\mu_{\text{arc}} \gtrsim 50$. This large magnification explains at least some of the untypical spectroscopic properties of cB58, e.g. that the star formation rate seems to be high and uniform and to take place in a large area.

Key words: Galaxies: fundamental parameters - Galaxies: clusters: individual - Cosmology: gravitational lensing, dark matter

1 INTRODUCTION

The $z = 2.72$ galaxy cB58 – discovered by the (ground-based) CNOC-survey of cluster redshifts (Carlberg et al. 1996a,b) – is one of the brightest ($m_V \approx 20.6$) high-redshift galaxies presently known. According to Yee et al. (1996, in the following Y96) the galaxy is a well resolved $3'' \times 2''$ disk-like galaxy, and thus, also the size of the galaxy is surprisingly large for its redshift. Several strong absorption lines were identified in the restframe wavelength range of $1000\text{\AA} \leq \lambda \leq 2000\text{\AA}$, which are characteristic for a young

stellar population. Using multi-color photometry Y96 and Ellingson et al. (1996) investigated its spectral energy distribution in a broader range, i.e. between $\lambda = 5000\text{\AA}$ and $\lambda = 21000\text{\AA}$. From SED-models of Bruzual & Charlot (1993) they inferred that a substantial fraction of the stellar component of the galaxy is younger than 10 Myrs, and that the extinction-corrected and model-dependent star formation rate has to be of order $4700 M_{\odot} \text{yr}^{-1}$. Due to the homogeneous appearance of the galaxy, the stars have to form uniformly in the galaxy. Thus, they conclude that cB58 is a galaxy in its initial star formation stage and call it a ‘protogalaxy’. A large magnification by gravitational lensing which would decrease the ‘true’ magnitude, size and star-formation rate of the galaxy was discarded as unlikely due to the ‘resolved, regular and smooth nature of the object’.

[★] Based on observations made with the NASA/ESA Hubble Space Telescope, obtained at the Space Telescope Science Institute.

Since the galaxy cB58 lies only $6''$ away from the central galaxy of the cluster MS 1512+36 at $z = 0.373$, Williams & Lewis (1997, in the following WL) investigated the possibility that cB58 is a ‘normal’ $z \approx 3$ star-forming galaxy magnified by the cluster. According to WL a magnification of $\mu \approx 40$ is sufficient to decrease the observed non-extinction corrected star-formation rate of $400M_{\odot}\text{yr}^{-1}$ to that value found by Steidel et al. (1996a) for $z > 3$ galaxies and by Ebbels et al. (1996) for arcs in galaxy clusters. The mass distribution of the cluster was modeled as an isothermal sphere with a core. A velocity dispersion of $\sigma = 1000\text{km/s}$ and a core radius of $22''.2$ provides a (fine-tuned) model for the mass distribution with a large magnification of $\mu \approx 40$ but a small shape distortion at the position of cB58, and avoids the prediction of multiple images, which were not observed from ground.

The velocity dispersion used in WL is in conflict with the measured value of $(690 \pm 100)\text{km/s}$ by Carlberg et al. (1996a), with a 90 percent confidence interval of $602 \leq \sigma/\text{km/s} \leq 840$ (Carlberg, private communication). The core radius of $\approx 140h_{50}^{-1}\text{kpc}$ exceeds that of the most detailed modeled and more massive clusters, e.g. A370 (Mellier et al. 1990, Kneib et al. 1993) or A2218 (Kneib et al. 1994, 1996) by 50 percent and a factor 3.5, respectively.

In this paper we present two color WFPC2 HST-observations. In contrast to the ground based data used by Y96 one can infer from the high-resolution WFPC2 data that although the cluster is poor in terms of velocity dispersion and optical richness, it is able to strongly distort and produce multiple images of high-redshift galaxies, and that cB58 is a gravitational fold arc. In section 2, 3 and 4 we describe the observations, the observed properties of the cluster, of some of its galaxies, and of all multiple image systems found. The positions of the multiple images are used for the lens modelling in section 5, where also limits on the magnification of the counterimage of cB58 are derived. The magnification of the arc cB58 is estimated in section 6. Section 7 provides a weak lensing analysis which serves as a consistency check for the estimated velocity dispersion. The results are summarized and discussed in section 8.

2 OBSERVATIONS

The cluster MS 1512+36 was observed with HST as part of a program to study the evolution of the Fundamental Plane of elliptical galaxies as a function of redshift and to constrain the geometry of the Universe (Bender et al. 1997). A detailed description of the corresponding results can be found in Saglia et al. (1997). Using the WFPC2 and the filters F555 and F675, three orbits were cumulated for each filter for a total of 6.3 and 5.8 Ksec, respectively. The exposure time was split in nine dithered images per filter to increase the resolution of the final image. Three sets of three images were taken, with horizontal integer pixel shifts between the three images and vertical subpixel ($1/2$ and $1/4$ of the WF pixel size) shifts between the sets, to allow an optimal cosmic ray rejection. The pipeline reduction was checked to be adequate. The images with integer pixel shifts were combined

using the cosmic ray rejection IRAF[†] algorithm, rebinned to a pixel size of one quarter of a WF pixel, aligned, averaged and rebinned to a pixel size of half a WF pixel, i.e. $0''.0498$. The zero-point photometric calibration was computed following Holtzman et al. (1995) and found to be in agreement with ground based photometry of the cluster (Ziegler 1996, 1997). The subsequent reduction was performed using MIDAS. The isophote shape analysis of the central cD galaxy allowed to determine a first estimate of the position of the major axis of the cluster potential, using the algorithm of Bender & Möllenhoff (1987), adapted to the HST resolution. A model for the light distribution of the cD galaxy was constructed from the isophote shape analysis and subtracted from the images.

The magnitudes and colors of the gravitationally lensed galaxies described below were derived from these frames computing both aperture photometry with appropriate apertures and annuli for the estimation of the sky value, and isophote magnitudes. Table 1 gives the magnitudes and colors inside the $24.78\text{ mag/arcsec}^2$ isophote in the V and $24.71\text{ mag/arcsec}^2$ isophote in the R band, corresponding to the $3 - \sigma$ limit above the sky. The errors are computed from the isophote magnitudes above 2 and $4 - \sigma$ above the sky and reproduce the observed variations in the aperture magnitudes due to photon statistics of when different galaxy or sky apertures are used.

The Lucy-Richardson deconvolution algorithm (Lucy 1974) as implemented in MIDAS was applied to enhance the resolution across the gravitational arc cB58. Twenty iterations were performed using the PSF generated by TINY-TIM.

With the exception of the cD galaxy, all galaxy shapes were estimated using SExtractor (Bertin & Arnouts 1996).

3 THE CLUSTER AND THE CD-GALAXY

Fig. 1 shows the core of the cluster MS1512+36 using coadded V- and R-data. The cluster is dominated optically by its cD galaxy (center of Fig. 1). The measured velocity dispersion of the cD galaxy equals $260 \pm 20\text{km/s}$, and increases to $\sigma_{cD} = 286 \pm 20\text{km/s}$ after aperture correction (Ziegler & Bender 1997). The results of the isophote shape analysis of the cD galaxy are shown in Fig. 2.

Note that the position angle and eccentricity of the light from the halo of the cD are not constant but both increase in the outer parts of the cD. From Fig. 2 we derive an axis ratio and major axis of the cD of $r = b/a = 0.7$ ($r = 0.6$) and $\phi = 10^\circ$ ($\phi = 6^\circ$) at a distance of $4''$ ($7.5''$) from its center (angles are counted with respect to the x-axis of the WFPC 3-chip). The major axis of the cD galaxy and that of the cluster potential – as inferred from X-ray photons – are roughly in agreement (compare with the X-ray map in Hamana et al., 1997). Similar to the optical data the X-ray map shows also a twist of the isophotes and an ellipticity change of the X-ray contours.

[†] IRAF is distributed by the National Optical Astronomy Observatories which is operated by the Association of Universities for Research in Astronomy, Inc. under contract with the National Science Foundation.

There is a face-on blue spiral galaxy with $m_V = 21.08$ and $m_{V-R} = 0.48$ at a distance of 4 arcseconds from the cD galaxy. Absorption of the light from the halo of the cD near the spiral arms suggests that the spiral is in front of the cD. With only one color it is quite difficult to estimate its photometric redshift. However, the irregular morphology of the galaxy, characterized by very bright and numerous H II star forming regions allows us to put some constraints on its spectral type and star formation history. We modeled the galaxy's stellar population using the GISSEL library for solar metallicity and Salpeter IMF (Bruzual & Charlot 1997), assuming an exponentially decreasing star formation rate $\psi(t) = \tau^{-1} \exp(-t/\tau)$ with different time scales ($7 < \tau < 10$ Gyr), and allowing for different return fractions for gas recycling (up to 40%). We have assigned an age of 10 Gyr to the galaxy and considered the evolution of its spectral energy distribution for a set of cosmological parameters ($H_0 = 50, 75 \text{ km/s/Mpc}^{-1}$, $q_0 = 0.01, 0.1$). There are many uncertain parameters in these models, like the IMF, metallicity, dust etc. However, all galaxy models we considered indicate that the observed $V - R = 0.48$ can be matched either at $z \leq 0.35$ or at $z \approx 0.9$. The exponential scale length of $1''.1 - 1''.3$ clearly excludes the second hypothesis and thus the most probable redshift is $0.25 < z < 0.37 \equiv z_{cl}$. For this redshift range the R magnitude corresponds approximately to the rest frame V magnitude and the luminosity of the galaxy is $0.8L_* \leq L \leq 1.8L_*$.

4 MULTIPLE IMAGES

Although the cluster is optically poor and dynamically weak, there are several strong and weak lensing signatures visible:

i) As described by Y96, the galaxy cB58 (also denoted by A1 in the following) is at $5''$ distance from the center of the cD; its V- and R-band magnitudes are $m_R = 20.29$ and $m_V = 20.64$, and its major-axis position angle is $\phi_{A1} = 71.6^\circ$. The galaxy is more elongated than visible from the ground (compare with Fig. 2 in Y96). Its light distribution is slightly curved, with the center of curvature not coinciding with the position of the cD, but pointing towards the outskirts of the cluster. Fig. 3 shows the Lucy-Richardson deconvolved light distribution of cB58 in the R-band. The local background and rms-noise are 1.2 and 0.4 counts per pixel, respectively; hence the limiting contour of 5 counts per pixels is 9.5 sigma above the background and the light distribution inside this contour is hardly affected by background noise. The mirror symmetry of the light distribution (the symmetry axis is sketched by the dashed line) indicates that cB58 is a merged image pair of a gravitationally lensed source. The gravitational arc is very elongated and only marginally resolved in width: perpendicular to the major axis the flux distribution of the galaxy is confined to 4-5 (dithered) pixels, and the flux increases steeply from the boundary towards the major axis. At the contour level of 5 counts per pixel, the extent of the galaxy parallel to the major axis is about 50 pixels. The SExtractor axis ratio obtained from the (8) isophote-weighted second moments of the light distribution (within the same contour as limiting isophote) is about 7. The unweighted ratio of the outermost isophote is about 1 : 10. This axis ratio also places a lower

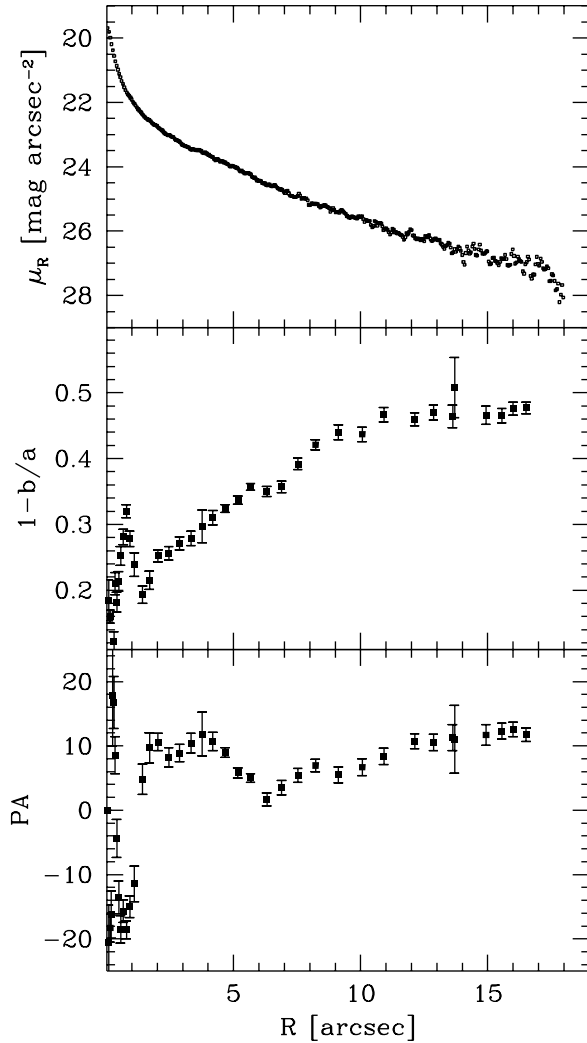


Figure 2. The isophote shape analysis of the cD galaxy. The top panel gives the circularly averaged surface brightness profile in the R band. The panel in the middle shows the ellipticity profile as a function of the circularized distance from the centre $R = \sqrt{ab}$. The panel at the bottom shows the position angle profile in degrees as a function of R .

limit on the magnification of the arc, together with its unresolved width and assuming that the source of A1 is spherical. The area enclosed by pixels with a surface brightness larger than 4 (5.5,10) counts per pixel is equal to 258 (210,138) pixels.

ii) There are several indications that the faint galaxies (B1, B2 in the following) at $8''$ distance from the cD-galaxy belong to a multiple image system: The galaxies have similar morphologies (see Fig. 4) and the same colors within the quoted errors (see Table 1). Third, there is a diffuse emission connecting the two galaxies, as expected when a faint part of the source lies on a caustic and thus is mapped into a gravitational arc, whereas the major part of the source is inside that caustic and is mapped into two images separated by the corresponding critical line. From the $V - R \approx 0.2$ color of B1 and B2 and from the reasonable assumption of their

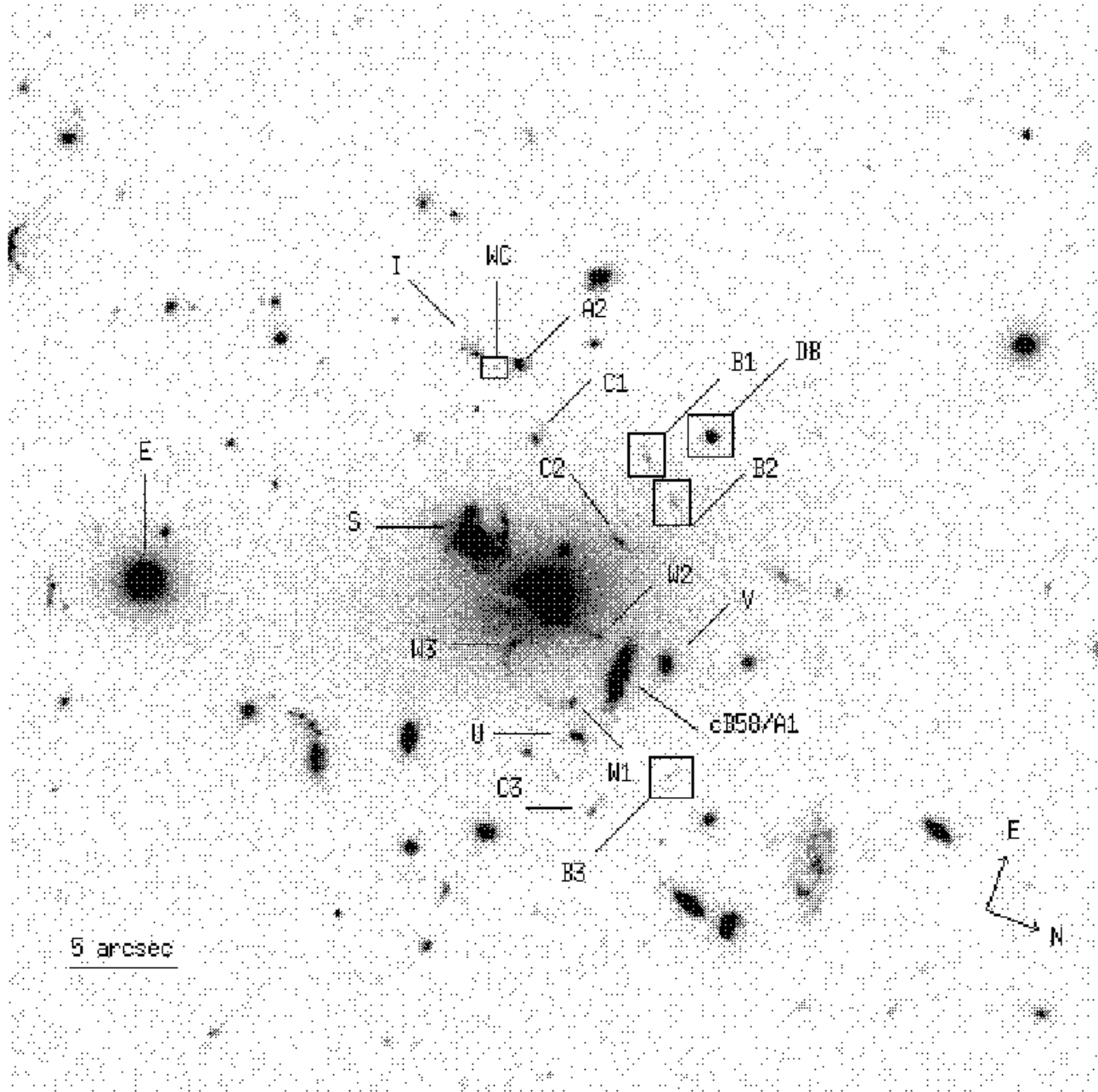


Figure 1. Image of the core of the cluster MS1512+36 using coadded V- and R-data. Close to the cD galaxy in the center is a face on spiral S to its left. The galaxy cB58 is on the opposite side at $5''$ distance with an inclination angle of 71.6° relative to the x-axis. The compact bright object A2 at $(r, \phi) \approx (11'', 97^\circ)$ is the counterimage of the gravitational arc cB58. Left to the upper and lower end of cB58 are two shrimp-like objects (W1 & W2) with their heads pointing towards cB58. As argued in the text, they are also lensed, with a counterimage WC left of A2, and a fourth image at W3. Near the upper right diagonal of the field there is the galaxy pair B1 & B2 (see also Fig. 4). The counterimage candidate B3 with polar coordinates $(r, \phi) \approx (10'', -56^\circ)$ relative to the cD is marginally visible in this Figure (see also Fig. 4). The three galaxies C1, C2 and C3 are most likely also multiply imaged galaxies.

morphological (spiral) type we estimate $z_B > 1.5$ as a lower limit for their redshifts with the GISSSEL models as above. The upper limit is $z_B < 5$ since otherwise the galaxies rest-frame Lyman-limit would drop out of the observers V-band. The elliptical galaxy (DB) $3''.2$ apart from B1 coincides in

color (see Table 1) with that of spectroscopically confirmed cluster members (e.g. the elliptical E and the cD galaxy; for details about spectroscopy of cluster members see Carlberg et al. 1996a&b, Ziegler & Bender 1997). The D_n - σ -relation (Dressler et al. 1987) yields an estimate of 84 ± 15 km/s for

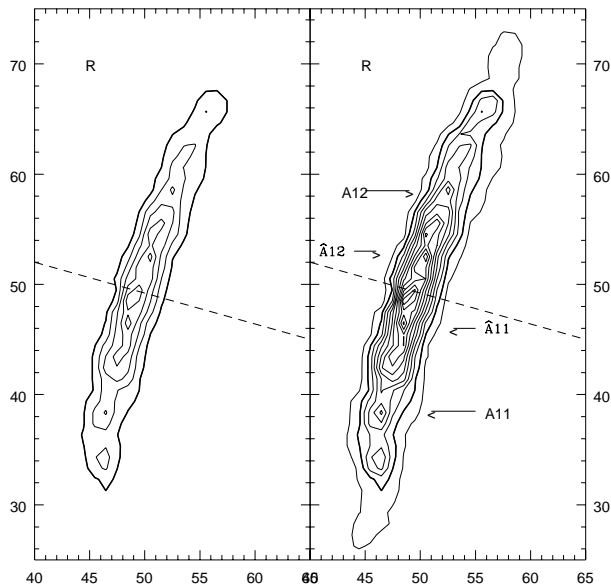


Figure 3. R-band counts for the galaxy cB58 obtained from the Lucy-Richardson deconvolved data. One unit in the horizontal and vertical direction equals one pixel of size $\approx 0''.05$. Contours are spaced by 10 (left) and 5 (right) counts per pixel; the thick line corresponds to 10 counts per pixel. The knots marked by A11 & A12, $\hat{A}11$ & $\hat{A}12$ are used for the lens modelling later on.

its velocity dispersion. Hence, the galaxy DB is separated by about 22 Einstein radii from B1 and its light deflection on B1 and B2 could be neglected in the field or in regions where the cluster is weak. Nearby a critical line, however, the small shear induced by DB is sufficient to perturb it locally and thus to change the magnification and (slightly) the positions of B1 and B2. Therefore, the galaxy DB will be taken into account in the quantitative lens modelling below.

The cluster potential determines the global properties of the tangential critical line of the lens systems (like the enclosed area and its approximate shape), whereas the massive cD galaxy and small galaxies near the critical line can perturb it only locally. Although the redshift of the galaxies B1 and B2 is not known, one can conclude that the cluster potential must be quite asymmetric already from the positions of the arc A1 and the galaxies B1 and B2: On the one hand, one could account for the fact that the direction and curvature of the arc is not in agreement with a spherically symmetric model by assigning sufficient lensing strength to the small galaxy V to the right of A1, perturbing the critical line and adding additional shear. On the other hand, if the cluster is spherically symmetric and has a small core radius as usually found for non-massive clusters (Mellier et al. 1993), the position of A1 indicates the Einstein radius of a $z = 2.7$ source, and the separation of the B1 and B2 system from the cD center (which is assumed to agree with the cluster center) measures the Einstein radius for the B1 and B2 source. Under the assumption of spherical symmetry

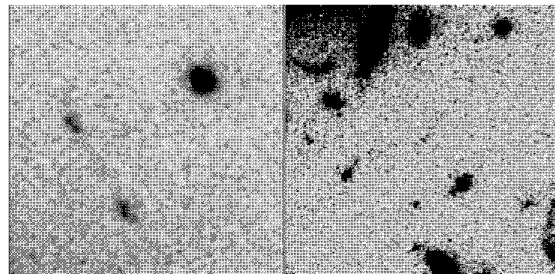


Figure 4. The left panel shows the pair of galaxies B1 (upper one) and B2 (lower one) which is at $8''$ distance from the cD galaxy. Their morphology and colors are identical and a diffuse emission is connecting them. The elliptical galaxy DB next to B1 and B2 will slightly perturb the tangential critical line caused by the smooth cluster potential. In the center of the right panel the counterimage candidate B3 is visible. It is barely resolved, but shows an additional diffuse emission which could correspond to the ‘arc’ connecting B1 and B2.

the ratio of these two Einstein radii is $1.4 - 1.6$ and it then describes the angular diameter distance from the cluster to the source of B1 and B2 in units of the angular diameter distance from the cluster to cB58 at $z = 2.7$. Since cB58 is at a high redshift already, such a high ratio can not be achieved for reasonable cosmologies, eg. $\Omega + \lambda = 1$ with $\lambda \leq 0.7$. If the core radius is non-negligible relative to the Einstein radius and is of the order of 6 to 7 arcsec as found by Hamana et al. (1997), the ratio of the Einstein radii drops to about 1.2 which is still too large to be accounted for by spherical symmetry.

The parameters of a lens system can be determined most accurately if the corresponding counterimages of arcs or double images on the opposite side of the cluster are found, because this determines the enclosed mass most strongly (see eg. Mellier, Fort & Kneib 1993 for MS 2137-23, Kneib et al. 1994, 1996 for Abell 2218). Modelling the cluster as an elliptical non-singular isothermal potential, and the cD as an elliptical singular isothermal potential and fitting the positions of the arc A1 and the pair B1 and B2 (with unknown redshift) we can predict the positions of the counterimage of A1 (denoted by A2) and that of B1 and B2, denoted by B3. Comparing to the observations we identify a galaxy as the counterimage A2 and a candidate for the counterimage B3.

iii) The galaxy A2 is the compact object at the upper boundary of Fig. 1 and, more expanded, the bright object at the right of Fig. 5. Its magnitudes are $m_R = 22.83$ and $m_V = 23.23$; it is the only object in that region where the counterimage is expected and whose color agrees with that of A1 (see Table 1). The galaxy to the left of A2 (denoted by I) is too blue to be the counterimage. The contours for the counts per pixel in the R- and V-band can be seen in the lower left and lower right part of Fig. 6. The high surface brightness core of A2 is unresolved. In the R-band, the surface brightness of 4 (5.5, 10) counts per pixel is only exceeded within 27 (16, 3) pixels. A comparison of the area enclosed by the same contours in A1 shows that the arc-area is ≥ 46 (approx. 13, approx. 10) times that of the counterimage for

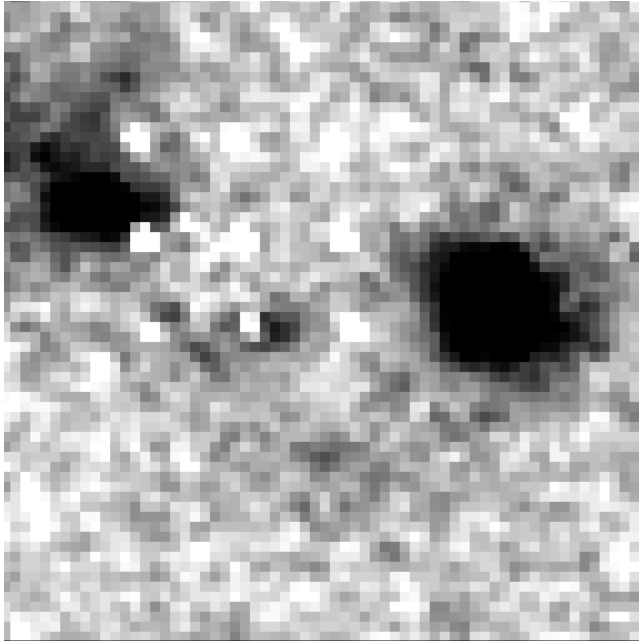


Figure 5. The right object in this part of the $V + R$ -coadded image is the counterimage A2 of the gravitational arc cB58; the left object (I) is considerably bluer than A2. The grid of nine white pixels is caused by one bad pixel and reflects the nine different dither positions in the coadded $V + R$ -exposures. The small object (WC) between A2 and I has a morphology similar to the ‘shrimps’ W1 and W2 visible in Fig. 1 and Fig. 7. We consider this as the counterimage candidate of W1 and W2.

contours of 10 (5.5,4) counts per pixel. From the magnitudes of A1 and A2 we obtain a magnification ratio of A1 to A2 of $\mu_{A1/A2} \approx 11$. Hence we conclude that the high surface brightness core of the source of A1 and A2 lies on the caustic and is magnified most strongly, whereas the other remaining regions of the source are magnified only moderately, and parts of it are only singly imaged (into A2).

iv) The candidate B3 for the counterimage of B1 and B2 is the central object in the right panel of Fig. 4 which was obtained using coadded $V + R$ data. Since its flux is not much above the noise level in R, the magnitude there can be measured only with a large error; this is less severe in the V-band; the color of B3 agrees within the large errors with that of B1 and B2. The galaxy in the center of Fig. 4 (right panel) is the only object above the 5σ detection limit of $V = 28.2$ whose position and color is compatible with being the counterimage B3. Although there is a galaxy nearby B3 as bright as DB (but bluer) for the case of B1 and B2, the additional light deflection caused by this galaxy will not be considered, since the cluster is non-critical at B3.

v) To the left of the upper and lower end of cB58 (see Fig. 1) are two shrimp-like objects (the lower (upper) one is denoted by W1 (W2)) pointing with their ‘head’ towards cB58. These two images have different parity and they are on opposite sides of the critical line defined by the flux distribution of the arc (see Fig. 3). Hence, a lensing interpretation is most natural, and it suggests that the source redshift is similar to that of cB58. Simple lens models (using the posi-

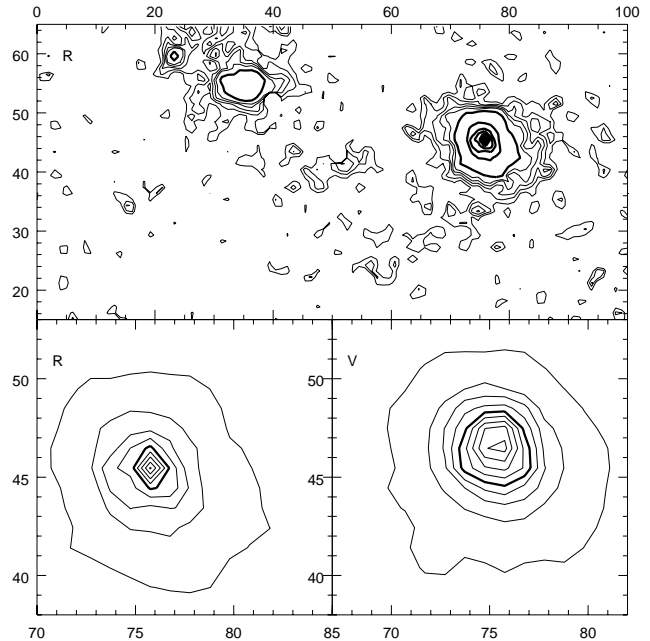


Figure 6. The upper part of this figure shows R-band contours of counts per pixel within the approximately same region as seen in Fig. 5. The thin curves represent low signal-to-noise contours with 1.35, 1.45, 1.55, 1.65 and 1.75 counts per pixel; the object WC

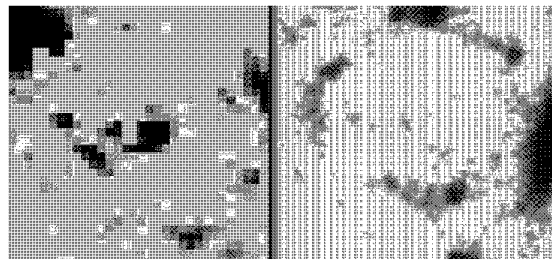


Figure 7. In the left panel one can see the counterimage candidate WC; although the signal-to-noise for this object is low (even in the coadded $V + R$ data), one can identify the same shrimp morphology (‘head’ to the right and curved ‘tail’ to left) as it is seen in the objects W1 (lowest object), W2 (right object) and W3 (left object) in the right panel, where a model for the emission of the cD galaxy was subtracted.

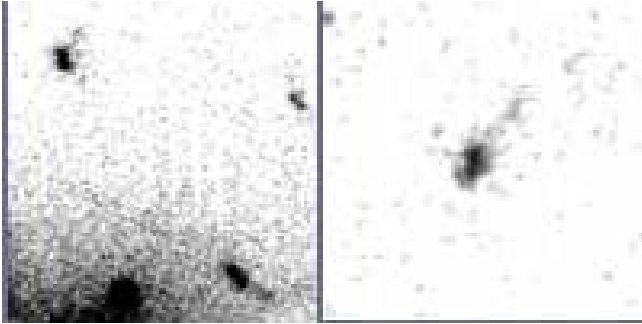


Figure 8. In the upper left and lower right corner of the left part of this figure C1 and C2 are visible. The suggested counterimage C3 (right part of the figure) coincides in morphology with C1 and C2: all objects consist of a ‘head’ and a ‘tail’ inclined to the major axis of the head. The parity of C1 and C2 is reversed. The relative orientation of the tail is predicted by lens models.

tions of A1 and A2, B1 and B2 to determine the parameters of the cD and the cluster) indeed *predict* that W1 and W2 have a common source and a faint counterimage left to A2 if they are at the same redshift as A1. They also predict a fourth image (W3 in the following) to the left of W1 and W2 right at that point of blue emission which makes the W-system to appear as a circular structure. The position of the fifth image depends more on the details of the model: eg., it can merge with the fourth image causing the more extended ‘head’ of W3, or it could be a fainter image near the center of the cluster. We can also identify the predicted counterimage of the W-system with a noisy emission between the I and A2-galaxies in Fig. 5 (WC in the following). More details of the W-system are given in Fig. 7 (using $V + R$ data). The left panel of this figure shows that the object WC is also ‘shrimp-like’ and has the same parity as W1. Since the fluxes of W1, 2 and 3 in the R-band are considerably affected by the red light of the cD galaxy, color comparisons are difficult. As described before, a model for the light distribution of the cD galaxy was constructed from the isophote shape analysis and subtracted from the images. But especially near W3 the color estimates may be affected by dust absorption due to the nearby spiral. For W1, 2 and WC the colors agree within the error bars, which do not include systematic errors due to insufficient subtracted cD light. We conclude that the ‘true’ color of the W-system is likely to be that of W1 or WC, whereas W2 and W3 may be affected by inaccurate subtraction of the cD light.

vi) The three galaxies C1 to C3 in Fig. 1 are most likely multiply lensed as well. C1 and C2 are on the opposite sides of the critical line for a $z \approx 2 - 3$ galaxy as it can be seen from an extrapolation of the critical line passing through B1 and B2 to the left. All of the three galaxies have a ‘head’ and a ‘tail’ inclined to the major axis of the head (see Fig. 8). C2 has opposite parity as C1 and C3. The colors of C1 and C3 do not support the lensing hypothesis (Table 1) because they only marginally agree within their $1-\sigma$ errors. The ground-based data in the B-band (Gioia & Luppino, 1994) provided by G. Luppino neither contradict nor confirm the lensing hypothesis further; although C1, C2 and C3 are all visible

Table 1. R- and V-magnitudes of objects as defined in the text (see Fig. 1).

Object	m_R	Δm_R	m_V	Δm_V	$V - R$
A1	20.29	+0.01, -0.03	20.64	+0.02, -0.02	0.41
A2	22.83	+0.04, -0.07	23.23	+0.05, -0.06	0.40
B1	25.77	+0.27, -0.31	26.08	+0.16, -0.37	0.31
B2	25.69	+0.29, -0.25	25.90	+0.24, -0.26	0.21
B3	28.42	+1.64, -1.30	27.58	+0.45, -0.71	-0.84
I	24.08	+0.19, -0.18	24.22	+0.18, -0.22	0.27
C1	24.60	+0.20, -0.23	24.66	+0.20, -0.22	0.06
C2	24.98	+0.21, -0.21	24.98	+0.19, -0.19	0.00
C3	24.95	+0.28, -0.25	25.58	+0.17, -0.33	0.63
W1	24.42	+0.28, -0.27	24.78	+0.34, -0.38	0.36
W2	25.82	+0.27, -0.26	25.61	+0.46, -0.49	0.79
W3	24.73	+0.30, -0.32	24.02	+0.44, -0.39	0.29
WC	26.89	+1.12, -0.55	27.04	+0.68, -0.60	0.15
U	23.66	+0.09, -0.13	24.16	+0.10, -0.12	0.50
V	22.96	+0.06, -0.09	23.30	+0.14, -0.10	0.34
DB	22.64	+0.03, -0.06	23.80	+0.04, -0.08	1.16
S	20.60	+0.03, -0.04	21.08	+0.04, -0.06	0.48

in the data, the exposure is not deep enough to improve the accuracy on the color determination. As the C-galaxies as well as B1 and B2 are visible in the B-band we can estimate the upper limit of their redshifts to about $z_{max} = 4$.

Despite the slight inconsistency of the colors of C1 and C3 we consider C1, C2 and C3 as a multiple image system: for every lens model which reasonably fits the A, B and W system we *robustly predict* that C1 to C3 have a common source if their redshift is marginally larger than that of cB58. Additionally, the directions of the tails relative to the major axis of the heads are also predicted as they are observed. Accidentally it may happen that three sources are along the line of sight to three possible multiple image positions, but we consider it unlikely, since not only their relative morphology but also their relative orientation agrees with that predicted by gravitational lensing.

5 MODELLING THE LENS SYSTEM

5.1 The deflection potential of the cluster and the galaxies

We model the deflection potential of the cluster, the cD-galaxy and of other individual galaxies by an elliptical non-singular isothermal deflection potential with a velocity dispersion σ , a core radius ζ , a major axis orientation angle ϕ and an ellipticity parameter ϵ [in units of km/s, (dithered) pixels, and degrees with respect to the x-axis],

$$\psi(\tilde{x}, \tilde{y}) = \psi_0 \sqrt{1 + q_\psi \left(\frac{\tilde{x}}{\zeta} \right)^2 + \frac{1}{q_\psi} \left(\frac{\tilde{y}}{\zeta} \right)^2}. \quad (1)$$

Here, \tilde{x} and \tilde{y} denote pixel positions with respect to the center of mass, the \tilde{x} -axis is parallel to the major axis of the

potential and $q_\psi =: (1-\epsilon)/(1+\epsilon)$ is the axis ratio of equipotential contours. The normalization $\psi_0 = \theta_E \zeta$ depends on the Einstein radius

$$\theta_E = 4\pi \left(\frac{\sigma}{c}\right)^2 \frac{D_{\text{ds}}}{D_s}, \quad (2)$$

where c is the speed of light while the source redshift and the cosmological parameters enter in the angular diameter distances from the cluster to the source (D_{ds}) and from the observer to the source (D_s). At redshift z the Einstein angle becomes

$$\theta_E \approx \left(\frac{\sigma}{49\text{km/s}}\right)^2 \frac{D_{\text{ds}}(z)}{D_s(z)} \left[\frac{D_{\text{ds}}(cB58)}{D_s(cB58)}\right]^{-1} \text{ pix} \quad (3)$$

for an Einstein-de Sitter universe and increases by a factor of ≈ 1.4 for a flat universe with $\Omega = 0.3$. Any value of velocity dispersions quoted below assumes an Einstein-de Sitter cosmology.

The deflection angle α , surface mass density κ , shear $\gamma = \gamma_1 + i\gamma_2$ and magnification μ of a point source can be obtained as first and second order derivatives of the deflection potential with respect to the angular coordinates \tilde{x} and \tilde{y} (Schneider, Ehlers & Falco 1992),

$$\alpha_i = \psi_{,i}, \quad \kappa = \frac{1}{2}(\psi_{,22} + \psi_{,11}), \quad (4)$$

$$\gamma_1 = \frac{1}{2}(\psi_{,22} - \psi_{,11}), \quad \gamma_2 = -\psi_{,12}, \quad (5)$$

$$\mu^{-1} = (1 - \kappa)^2 - |\gamma|^2. \quad (6)$$

With $C := \psi/\psi_0$, $Q := (q_\psi + 1/q_\psi)$ and $\bar{Q} := (1/q_\psi - q_\psi)$ these functions become

$$\kappa = \frac{1}{2C^3} \left\{ Q + \frac{\tilde{x}^2 + \tilde{y}^2}{\zeta^2} \right\} \frac{\theta_E}{\zeta}, \quad (7)$$

$$\gamma_1 = \frac{1}{2C^3} \left\{ \bar{Q} + \frac{\tilde{x}^2 - \tilde{y}^2}{\zeta^2} \right\} \frac{\theta_E}{\zeta}, \quad (8)$$

$$\gamma_2 = \frac{1}{2C^3} \left\{ \frac{2\tilde{x}\tilde{y}}{\zeta^2} \right\} \frac{\theta_E}{\zeta}. \quad (9)$$

The mass distribution has the following properties:

1. It simplifies to the mass profile of a singular isothermal sphere, $\kappa \approx \frac{\theta_E}{2\sqrt{\tilde{x}^2 + \tilde{y}^2}}$, if the mass distribution is spherically symmetric ($q_\psi = 1$) and if positions with $\tilde{x}^2 + \tilde{y}^2 \gg \zeta^2$ are considered.

2. For an isopotential axis ratio q_ψ the mass within an ellipse of the same axis ratio q_ψ and area πr^2 equals

$$M_r(q_\psi) = \pi\theta_E\zeta \left\{ \frac{Q - 1 + \frac{Q}{2}\left(\frac{r}{\zeta}\right)^2}{\sqrt{1 + \left(\frac{r}{\zeta}\right)^2}} + 1 - Q \right\}. \quad (10)$$

Hence, for an elliptical potential the ratio of the mass within an ellipse of axis ratio q_ψ and area πr^2 to the mass $M_r^0 := M_r(q_\psi = 1)$ within a circle of radius r and a circular potential is given by

$$\frac{M_r(q_\psi)}{M_r^0} = \frac{Q - 1 + \frac{Q}{2}\left(\frac{r}{\zeta}\right)^2 + \sqrt{1 + \left(\frac{r}{\zeta}\right)^2} [1 - Q]}{1 + \left(\frac{r}{\zeta}\right)^2 - \sqrt{1 + \left(\frac{r}{\zeta}\right)^2}}; \quad (11)$$

this ratio equals one at $r = 0$, increases monotonically with increasing r and becomes

$$\lim_{\left(\frac{r}{\zeta}\right) \rightarrow \infty} \frac{M_r(q_\psi)}{M_r^0} = \frac{1}{2}Q = \left[q_\psi + \frac{1}{q_\psi} \right] \frac{1}{2} \gtrsim 1 \quad (12)$$

for $r^2 \gg \zeta^2$. Thus models with the same velocity dispersion σ but different ϵ have different isodensity shapes but the same ‘mean’ mass density (measured within ellipses with an axis ratio given by the potential). We want to point out that the ‘velocity dispersion’ σ derived from the amplitude $\psi_0 = \theta_E\zeta$ has a straightforward relation to the observed velocity dispersion of cluster galaxies only in the spherical symmetric case. Nevertheless we will express the estimated amplitude in terms of velocity dispersion of the cluster later on.

3. For small eccentricities of the cluster potential $\epsilon_{\text{cl}} < 0.2$ the isodensity contours are roughly elliptical and the axis ratio

$$q_\kappa =: \frac{1 - \hat{\epsilon}_{\text{cl}}}{1 + \hat{\epsilon}_{\text{cl}}} \quad (13)$$

of the isodensity contours is related to the isopotential contours according to $\hat{\epsilon}_{\text{cl}} \approx 3 \epsilon_{\text{cl}}$.

The lens models investigated below are described by the following parameters:

1. The orientation ϕ_{cl} , ellipticity ϵ_{cl} , velocity dispersion σ_{cl} and the core radius ζ_{cl} of the cluster will be treated as free parameters. The cluster center is assumed to coincide with that of the cD-galaxy.

2. The ellipticity and orientation of the cD galaxy are either treated as free parameters, are assumed to be equal to that of the cluster or inferred from the light. In the second case the assumption is motivated by earlier investigations (eg., Mellier et al. 1993) finding that the major axis of clusters dominated by a single mass concentration is aligned with that of the central galaxy. In the third case we assume that the surface brightness distribution of the extended diffuse emission of the cD traces its surface mass density. Using equation (13) we obtain $\epsilon_{\text{cD}} = 0.06 - 0.08$ and $\phi_{\text{cD}} = 5^\circ - 10^\circ$. The core radius is assumed to be zero, whereas the velocity dispersion σ_{cD} of the cD-galaxy is a free parameter.

3. Additional galaxies are treated as spherical singular systems ($\epsilon = 0$, $\zeta = 0$) with their velocity dispersion as free parameters.

5.2 The lens models

Let $\vec{p} = (p_1, \dots, p_f)$ denote the free parameters of the lens model, K the number of multiply lensed sources, $I(k)$, $k = 1, \dots, K$ the number of images for each of the k sources; further, let $\vec{\theta}_{i_k}$ denote the position of the i^{th} image ($1 \leq i_k \leq I(k)$) of the k^{th} source. For each image position the deflection angle $\vec{\alpha}(\vec{\theta}_{i_k}; \vec{p})$ is calculated and a source position $\vec{\beta}_{i_k}(\vec{p}) := \vec{\beta}(\theta_{i_k}; \vec{p}) = \vec{\theta}_{i_k} - \vec{\alpha}(\vec{\theta}_{i_k}; \vec{p})$ is predicted. The best fitting model is obtained by minimizing

$$E := \sum_{k=1}^K W(k) \sum_{i_k, i'_k=1}^{I(k)} w(i_k)w(i'_k) \left| \vec{\beta}_{i_k} - \vec{\beta}_{i'_k} \right|^2 + f(P) \quad (14)$$

with respect to the free parameters of the model using the `powell` routine described by Press et al. (1992). $W(k)$ and $w(i_k)$ are weights equal to one or zero, and thus they determine which of the multiply imaged sources are considered

($W(k)$), and which of their images ($w(i_k)$) are taken into account for the model fitting. The additive function $f(P)$ is used to take into account parities P of images. (The photometry is too inaccurate to include flux ratios.)

The fold arc contains much more information than the position of its center of light: the critical line passes through it and each pixel must have a corresponding one with the same surface brightness on the opposite side of the critical line, and these pixel pairs will have a common source in the ideal case. The information contained in the light distribution of the arc will be used in more detail later on; if we only fit the position of the arc we simply choose two of these corresponding points (A11 and A12) on opposite sides of the critical line, require that they and A2 have a common source (A) and that the parity of A11 and A12 is reversed. We used the positions of the knots (which have the same surface brightness) marked in Fig. 3 as A11 and A12. The use of the A11 and A12-positions together with the parity constraint requires the critical line to pass between A11 and A12, e.g., it rejects models where A11 and A12 belong to the same large segment of a giant tangential arc. The parity constraint is easily implemented by adding a term to (14) proportional to the product of the determinant of the Jacobians if this product is positive.

Thus, generally four kinds of observables can be used for the model fit: positions (A11, A12, A2, B1, B2, B3, W1, W2, WC, W3, C1, C2, C3), flux ratios, the parity of the lens map at A11/A12 and B1/B2 and the flux-distribution of the arc. In Table 2 one can read off all parameters used for the lens modelling, and whether they are varied (+) or kept constant (-). In the first case the number below the plus equals the best fit value, in the second case it equals the assumed fixed value. As discussed already, the lens model is described by the cluster (σ_{cl} , ϵ_{cl} , ϕ_{cl} and θ_{cl}), the cD galaxy (σ_{cD} , ϵ_{cD} , ϕ_{cD}), the possibly perturbing galaxies DB, V and S next to B1/B2, A1 and left of W3 (σ_{DB} , σ_V , σ_S), and the unknown lensing strengths

$$d_B := \frac{D_{ds}(B)}{D_s(B)} \left[\frac{D_{ds}(cB58)}{D_s(cB58)} \right]^{-1}, \quad (15)$$

$$d_W := \frac{D_{ds}(W)}{D_s(W)} \left[\frac{D_{ds}(cB58)}{D_s(cB58)} \right]^{-1}, \quad (16)$$

$$d_C := \frac{D_{ds}(C)}{D_s(C)} \left[\frac{D_{ds}(cB58)}{D_s(cB58)} \right]^{-1} \quad (17)$$

of the lens for B, W and C relative to cB58. Here $D_{ds}(X)$ and $D_s(X)$ are the angular diameter distances from the cluster to a source X and from the observer to the source. The starting values used in the minimization are given in the first line of Table 3. They are motivated by prior knowledge in the case of σ_{cl} , σ_{cD} and σ_{DB} : i.e. by the best fit value for the velocity dispersion of Carlberg et al. (1996a,b), the measurement of the velocity dispersion of the cD by Ziegler & Bender (1997), and the estimate of σ_{DB} using the D_n - σ -relation which gives 84 ± 15 km/s. If nothing else is stated we restrict the allowed range for the velocity dispersion of the cD in the minimization of (14) to $246 \text{ km/s} \leq \sigma_{cD} \leq 306 \text{ km/s}$ which is the 1 - σ interval for the observed uncorrected and aperture-corrected velocity dispersion of the cD. The ellipticity of the cluster and the cD is limited by $\epsilon_{cl} \leq 0.25$ and $\epsilon_{cD} \leq 0.2$. The role of the V-galaxy will be discussed later;

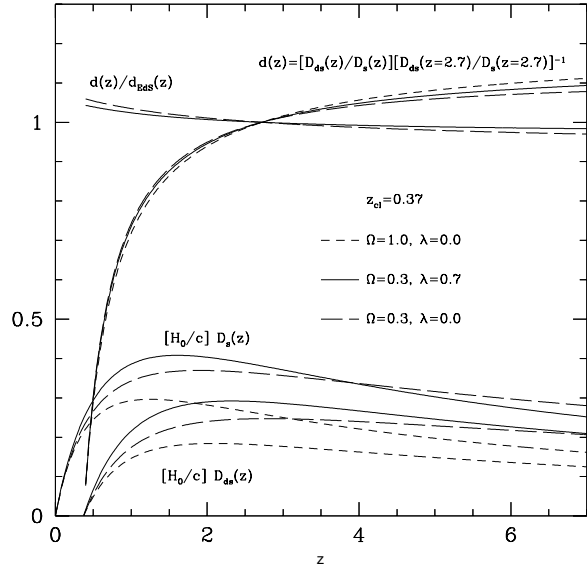


Figure 9. For three different cosmological models we have plotted the angular diameter distances from the observer (O) and the angular diameter distances from the cluster (C) to redshift z in units of the Hubble length (c/H_0): Einstein-de Sitter model (short-dashed), a low- Ω universe with $\lambda = 0$ (long-dashed) and with $\lambda = 1 - \Omega$. The redshift of the cluster is $z_{cl} = 0.37$. The remaining three curves which start at redshift $z = 0.37$ and are equal to zero there show the lensing strength D_{ds}/D_s of a galaxy at redshift z in units of the lensing strength of the galaxy cB58 at $z = 2.7$, for the same three cosmological models. This ratio is called relative lensing strength d further on. The two flat curves show the relative lensing strength for the two low- Ω cases in units of the relative lensing strength for an Einstein-de Sitter universe.

a velocity dispersion of $\sigma_V \leq 180$ km/s will be a safe upper limit irrespective of its redshift. The limiting values for d_B , d_W and d_C , $0.1 \leq d_X \leq 1.1$ only imply that the galaxies of the B, W and C-system are behind the cluster and below a redshift of five. To illustrate that, we have plotted the lensing strength for a galaxy at redshift z in units of the lensing strength for cB58 for three different cosmological models in Fig. 9 (for details concerning filled beam angular diameter distances see Fukugita et al. 1992, Asada 1996). In terms of lensing strength, a galaxy at $z = 2.7$ is almost at ‘infinity’ for a cluster at redshift $z = 0.37$; the lens is stronger only by 8% for a galaxy at redshift of five, nearly independent of the cosmological model assumed.

Minimizing E in (14) implies that the distances between the source positions – estimated for all the members of a multiply lensed system – are minimized in the source plane (In the ideal case the source separation is zero, because the galaxies are assumed to have a common source.) To estimate the quality of the best fitting model \hat{p} we define the ‘mean’ source for each image system as a disk with radius of half a pixel centered on

$$\hat{\beta}_k := \frac{1}{\sum_{i_k} I(i_k)} \sum_{i_k=1}^{I(k)} \vec{\beta}_{i_k}(\hat{p}) w(i_k) \quad . \quad (18)$$

With ray tracing we approximately invert the lens equation and solve for the extended images corresponding to the mean source. Let $\vec{\Delta}(i_k)$ be the minimum distance of $\vec{\theta}_{i_k}$ from the inverted extended images; we then define

$$\Delta_k^2 := \sum_{i_k=1}^{I(k)} |\vec{\Delta}(i_k)|^2 w(i_k) \quad (19)$$

as the quadratic error of the fit. This error (divided by the number of images used for the fit) has to be compared to the error of image localisation or the extent of the images at $\vec{\theta}_{i_k}$. Actually Δ_k^2 should be minimized with respect to \vec{p} to obtain the best fitting model. Instead of this time consuming process we minimize E (14) and assume that the parameters which minimize E are not too different from those which minimize Δ_k^2 . The fit quality of a model is quantified in Table 3. The first four columns contain the quadratic error of the fit in the lens plane which was defined in equation (19). If a multiple *image system* (A, B, W or C) is used for the fit, then the weights in (18) are equal to that used in the minimization; that means, if one of the multiple images of the system is not used for the fit, it is also not used to estimate the fit quality. If an image system is not used for the fit, then Δ^2 measures the quality of the prediction that the observed images have a common source; in this case (if nothing else is stated) all of its multiple image positions enter Eq. (19).

5.3 Results

The models explored followed a strategy of increasing complexity, aiming at assessing the robustness of the lensing predictions. The first models we investigated used the positions of A1/A2 and B1/B2 as observables; good fits predict that C1/C2/C3 and W1/W2/WC are multiple images; the exact position of W3 depends on the slope of the mass profile in the center; since W3 has the same ‘tail’ (in color and morphology) as W1, W2 and WC with reversed parity relative to W1, it is obviously a fourth image of WC, and it is used for further constraining the mass distribution in the core of MS1512+36. The observations show some evidence that the fifth image is merging ‘head on head’ with the fourth image (see Fig. 7). If this is the case then the radial critical line of the combined mass distribution (cluster and cD galaxy) passes through the head of W3. Alternatively, a slightly different redshift for A and W is sufficient to allow that an additional image of A (the existence of which is predicted for some of the models) lies next to the head of W3. Therefore we leave the fifth image position of the W-system unconstrained. Since the galaxy B3 is too faint for a precise measurement of its magnitude in R, and on the other hand is surprisingly bright relative to B1 and B2 (which are near a critical line and thus should be magnified considerably) we can not be absolutely sure that B3 is indeed the counterimage of B1 and B2. Consequently, we use as a first step only the positions of A1/A2, W1/W2/WC/W3, and C1/C2/C3 in the models M1a&b. In a second step (model M1Ia), we reverse the approach and check what happens when the positions of A1/A2, W1/W2/WC/W3, and B1/B2/B3 are used. In models M1IIa and M1IVa we explore the role of the slope of the potential. Models M1Va&b&c all the positions are used. With model M1Ia we investigate whether it is sufficient

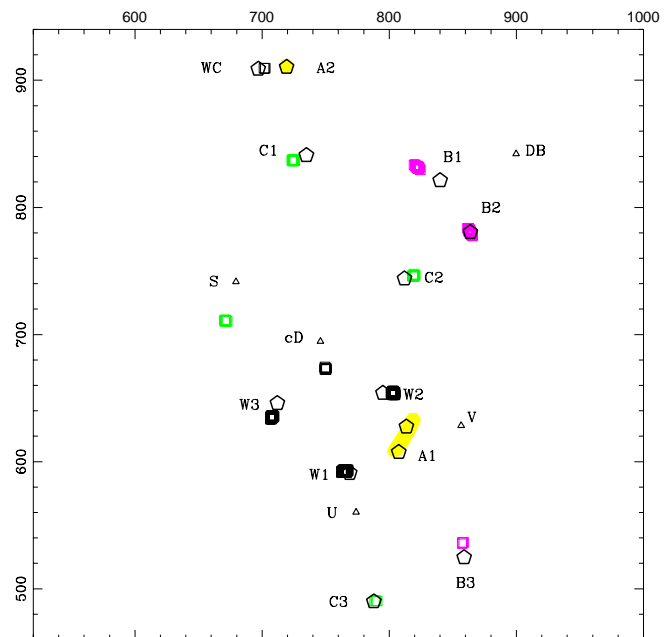


Figure 10. Observed positions of multiple images (hexagons) versus prediction (hatched regions) using the mean sources defined in (18). The best fitting model M1a was obtained using only the positions of the image system A, W and C and considering only the light deflection caused by the cD and the cluster as ‘free’ parameters. For more details, see text. To check the hypothesis that B3 is the counterimage of B1 and B2 we have inserted the additional images predicted for B2 assuming its redshift coincides with that of cB58.

to describe the lens system with the deflection potential of the cD, the cluster and DB, and whether models can be found where the potential depth of the cD galaxy is in agreement with its observed velocity dispersion. Hence the velocity dispersion of the cD is restricted to $246 \text{ km/s} \leq \sigma_{\text{cD}} \leq 306 \text{ km/s}$ (the 1σ -interval for the uncorrected and aperture-corrected velocity dispersion). The ellipticities of the cluster and cD potential are assumed to be smaller than 0.25 and 0.2, respectively; the velocity dispersion of DB is kept constant at $\sigma_{\text{DB}} = 84 \text{ km/s}$. The resulting best fit parameters are summarized in Table 2, and the predicted images of the mean sources can be seen in Fig. 10. The arc is curved a bit too strongly, but the position of the arc and its counterimage are fitted perfectly. From Figure 10 and Table 3 we infer that the positions of the predicted images of W (C) are off from the observed ones by 6.7 (6.9) pixels on average and thus the error is smaller than the typical extent ($\gtrsim 10$ pixels) of the images. To see whether B3 is indeed the counterimage of B2 and B1 we mapped the image B2 back into the source plane (assuming its redshift agrees with that of cB58) and we added the predicted images of that source in Fig. 10 as well. Since the positions of B1 and B2 were not used for the model fit one can not expect that the predicted position of B1 agrees with that of the observed one. The fact that the predicted third image of B is so close to that of the

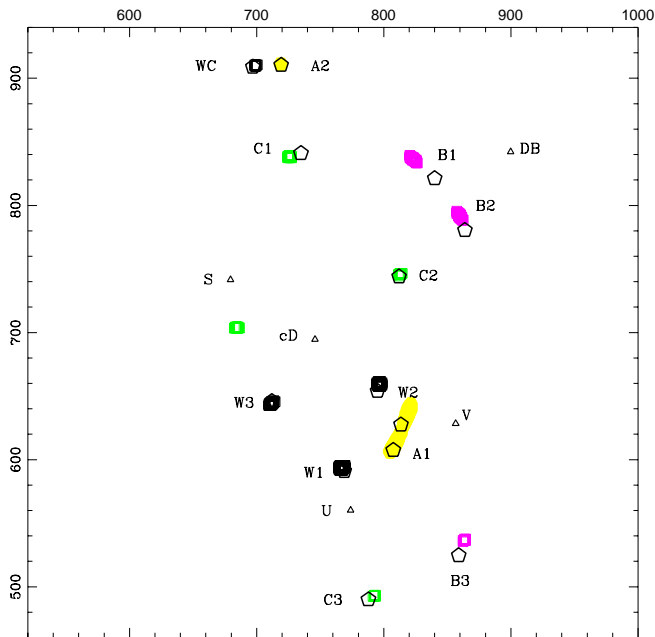


Figure 11. For the model M1b we used the arc positions $\hat{A}11$ and $\hat{A}12$ instead of A11 and A12. The remaining observables and the lens modelling is the same as for M1a. The arc becomes straighter (but also too long) and the W-system fit improves. We calculated the mean source of B1 and B2 and added the predicted images of that source. As before, the prediction is off from the observation by more than the extent of the galaxies B1-B3. However, it is obvious that B1 and B2 belong to a three image system, and that the third image is very close to the observed B3.

‘candidate’ B3 adds further weight to the hypothesis that B3 is the counterimage of B1 and B2.

To check the robustness of the best fit parameters we used the innermost two knots of cB58 (see Fig. 3, where they are marked as $\hat{A}11$ and $\hat{A}12$) instead of A11 and A12 for the fit. The resulting model is called M1b. The two knots together with the reversed parity at $\hat{A}11$ and $\hat{A}12$ constrain the critical curve at cB58 more strongly, because now the critical line must not only be somewhere between A11 and A12 but more confined between $\hat{A}11$ and $\hat{A}12$. The quality of the fit improves: the fit for the W and A system is almost perfect; the arc becomes straight due to the increased ellipticity ($\epsilon_{cD} = 0.199$) of the cD galaxy. The best fit parameters of M1a and M1b differ and they demonstrate that an increase of the velocity dispersion from ≈ 570 to 630 km/s can be compensated by an increase of the core radius from 120 to 180 pixels (which flattens the mass profile in the center). As far as the arc position and direction are concerned, a more circular cluster profile can be compensated by an increase of the ellipticity of the cD galaxy’s deflection potential.

We point out that taking into account flux ratios of multiple images can not resolve this ambiguity: objects near the critical line (B1, B2, A1) can not be considered, because their flux ratio depends on the details of the mass distribution near the critical line and they cannot be treated as

point sources. Thus, only for the objects C1, C2, C3 and W1, W2 and WC one can compare directly the magnification ratios predicted by the model with the observed flux ratios. From these objects, the magnitudes of W2 and C2 are affected by red light and absorption in V due to the cD galaxy (or by inaccurate subtraction of the cD light); since C1 and C3 differ in color by about 0.6, only W1 and WC remain as ‘clean’ sources. In the coadded data (which improve the signal-to-noise especially for WC) we obtain a magnitude difference of $\Delta_{C1}^W = 2.2 \pm 0.75$ for the objects WC and W1. The comparison of the predicted magnitude difference of the multiple images Δ_{21}^C , Δ_{31}^C and Δ_{C1}^W in Table 3 shows that the predicted flux ratios are similar and agree reasonably well with the observations, where again M1b is a slightly better fit. The magnification of A2 increases from 2.15 to 2.89 if one changes the parameters from M1a to M1b, since then the larger velocity dispersion provides a larger surface mass density (and shear) at A2.

Since the models M1a&b predict the counterimage of B1 and B2 very close to B3 we now use the same observables as for M1a and assume further that B1, B2 and B3 have a common source; the free parameters are as in M1b. The resulting best fit is denoted by M1Ia. The quality of the fit is good (see Table 3 and Fig. 12). The C-system is predicted very accurately if we use the value for $d_C \approx 1.03$ derived from M1a&b. Of course, a zero velocity dispersion for DB is unrealistic. It is not unexpected, however, that the best fitting value for the velocity dispersion is off from a reasonable one (say 84 km/s) because DB is relatively far away from the critical line. For a velocity dispersion of 84 km/s the shear (and surface mass density) from DB at B1/B2 is only about 0.02. One can not expect that describing the true deflection potential by the sum of two elliptical potentials provides an accurate fit not only for the observables in the core but also at the positions of B1 and B2 at the 2 percent level, since the ellipticity and the slope of the surface mass density is expected to change from the inner to the outer parts of the cluster. We have tested how large the deviation from the model potential must be to allow for a perfect fit for the positions of B1, B2 and B3, by applying the same model fit as in the case of M1Ia, but now allowing for a ‘negative’ mass at DB; a ‘negative’ mass corresponding to -70 km/s changes the shear and magnification locally by only 0.04 (relative to the +84 km/s-case) – which is unmeasurable by weak lensing methods – and improves the fit quality to $\Delta_B^2 = 9$ relative to M1Ia and dims the brightness of B1 and B2 relative to B3.

When the positions of the As, Ws and Cs are used for the model fit, the prediction for B is not as good as when the positions of the As, Ws and Bs are used to predict the Cs. The reason is that in the first case the mass profile is probed mainly in the central region, whereas in the latter case the larger distances of B1/B2/B3 allow to constrain the slope of the mass profile better. We demonstrate this with the model M1Ia, which was derived in two steps: Best fit values for the parameters describing the cD galaxy, the cluster and the redshifts were obtained as for M1b, but with a triple weight for the positions of C1, C2 and C3. Using these parameters, the velocity dispersion of DB and redshift of B were varied to optimize the predicted positions for the Bs as well. The best fitting values are $d_B = 1.02$ and

Table 2. Best fit values (+) and assumed fixed values (–) for the cluster, the galaxies and the redshift of the objects. Velocity dispersions σ_{cl} , σ_{cD} , σ_{E} are given in km/s. Major axis position angles Φ_{cl} and Φ_{cD} are given in degrees. The core radii ζ_{cl} are quoted in pixels – where one pixel corresponds to $0''.0498$. See Fig. 9 to convert the lensing strengths d_B , d_W , d_C into redshifts.

Model	σ_{cl}	ϵ_{cl}	ϕ_{cl}	ζ_{cl}	σ_{cD}	σ_{DB}	σ_{S}	σ_{V}	d_B	d_W	d_C	ϵ_{cD}	ϕ_{cD}	σ_{E}
start	710	0.0	8	100	286	84	0	0	1	1	1	0.06	10	176.0
MIa ^(1a)	+	+	+	+	+	–	–	–	–	+	+	+	+	–
MIa ^(1a)	569.1	0.1579	11.34	122.0	246.3	84	0	0	1.	1.002	1.048	0.0816	12.13	176.0
MIB ^(1b)	+	+	+	+	+	–	–	–	–	+	+	+	+	–
MIB ^(1b)	630.8	0.1091	6.465	181.3	251.4	84	0	0	1.	0.9998	1.026	0.1991	26.7	176.0
MIIa ⁽²⁾	+	+	+	+	+	+	–	–	+	+	–	+	+	–
MIIa ⁽²⁾	564.0	0.2023	12.14	141.0	246.0	0	0	0	1.025	1.0	1.03	0.0001	12.13	176.0
MIIIa ⁽³⁾	+	+	+	+	+	+	–	–	+	+	+	+	+	–
MIIIa ⁽³⁾	593.4	0.1797	9.73	158.27	249.1	72	0	0	1.020	1.0004	1.037	0.0	–	176.0
MIVa ⁽⁴⁾	+	+	+	+	+	–	–	–	–	+	–	+	+	–
MIVa ⁽⁴⁾	585.0	0.1894	12.19	152.5	247.0	84	0	0	1.020	1.005	1.035	0.0018	18.54	176.0
MVa ⁽⁵⁾	+	+	+	+	+	+	–	–	+	+	+	–	–	–
MVa ⁽⁵⁾	571.7	0.1753	11.77	144.9	268.4	70	0	0	1.024	1.001	1.042	0.06	10.00	176.0
MVb ⁽⁵⁾	+	+	+	+	+	+	–	–	+	+	+	–	–	–
MVb ⁽⁵⁾	583.2	0.1511	12.40	136.1	246.0	70	0	0	1.024	1.002	1.042	0.11	10.00	176.0
MVc ⁽⁵⁾	+	+	+	+	+	+	–	–	+	+	+	–	–	–
MVc ⁽⁵⁾	615.4	0.1407	11.68	166.6	246.0	70	0	0	1.023	1.004	1.035	0.06	ϕ_{cl}	176.0
MVIa ⁽⁶⁾	+	+	+	+	+	+	+	+	+	+	+	+	+	–
MVIa ⁽⁶⁾	582.0	0.1581	14.30	159.9	246.2	7	111	104	1.016	1.007	1.035	0.1301	12.22	176.0

(1a) Positions of A11/A12/A2, W1/W2/W3/WC, C1/C2/C3 fitted.

(1b) Positions of $\hat{A}11/\hat{A}12/A2$, W1/W2/W3/WC, C1/C2/C3 fitted.

(2) Positions of A11/A12/A2, W1/W2/W3/WC, B1/B2/B3 fitted.

(3) As (1a), with triple weight for C1/C2/C3.

(4) Positions of A11/A12/A2, W1/W2/W3/WC fitted.

(5) Positions of A11/A12/A2, W1/W2/W3/WC, B1/B2/B3, C1/C2/C3 fitted.

(6) Positions of A11/A2, W1/W2/W3/WC, B1/B2/B3, C1/C2/C3 fitted as well as the shape of the arc cB58.

Table 3. The quality of the best-fit models. The quantities Δ_W^2 , Δ_A^2 , Δ_C^2 , Δ_B^2 give the square position residuals (in pixels) as defined in Eq. 19; μ_2^A are the predictions for the magnification of A2 (counterimage of cB58); δ_{21}^C , δ_{31}^C , δ_{C1}^W , δ_{32}^B are the predicted magnitude differences for C2/C1, C3/C1, WC/W1 and B3/B2. The first line contains the observed magnitude differences in the V-band. The uncertainties for these magnitude differences can be obtained using table 1.

Model	Δ_W^2	Δ_A^2	Δ_C^2	Δ_B^2	μ_2^A	δ_{21}^C	δ_{31}^C	δ_{C1}^W	δ_{32}^B
Observed	–	–	–	–	–	0.33	0.92	2.26	1.68
MIa	179.2	0.5	144.4	–	2.153	0.196	0.674	1.63	1.05
MIB	20.6	4.0	79.51	396.8	2.894	0.337	0.775	1.79	0.799
MIIa	22.7	6.0	40.8	20.8	2.180	0.21	0.698	1.79	1.27
MIIIa	226.4	54.0	11.8	1.2	2.374	0.19	0.734	1.68	1.42
MIVa	41.3	1.0	118.5	352.7	2.281	0.17	0.693	1.72	1.2
MVa	74.7	5.0	62.0	190.1	2.291	0.23	0.673	1.64	1.17
MVb	46.2	10.6	101.3	269.3	2.323	0.16	0.681	1.66	1.11
MVc	85.3	0.04	54.0	278.1	2.766	0.20	0.79	1.92	1.19
MVIa	43.6	1.4	116.4	246.0	2.386	0.12	0.71	1.63	1.28

$\sigma_{\text{DB}} = 72$ kms/s. As expected (see Table 3) the quality of fit improves in the outer regions and decreases in the core.

Thus we have demonstrated that the numerous multiple images can be fitted at the same time with a very simple model consisting of a singular (non-singular) elliptical poten-

tial for the cD galaxy (and the cluster). The fact that the best fit parameters in Table 2 can be quite different from model to model shows that no fine tuning of the parameters is necessary to explain the multiple images. (However, model MIa&b is not a good fit for the image positions of the

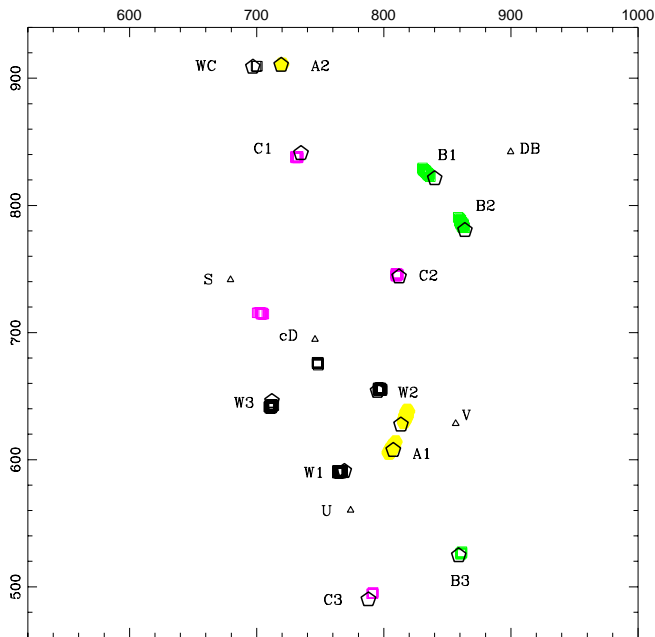


Figure 12. For this fit the free parameters of the lens model were the same as for M1a&b with an additional variation of the velocity dispersion of DB. Instead of the C-system the B-system was used for the fit. Assuming that $d_C = 1.03$ the mean source of C1, C2 and C3 is obtained and the predicted images of that source are also plotted.

B-system). The images C are most robust with respect to a change of the parameters, whereas the W and A galaxies are sensitive to the steepness and height of the combined potential (of course the contributions coming from the cD and the cluster can be varied), and the Bs are more sensitive to the ellipticity and slope of the potential at $\theta \geq 10''$.

5.4 The magnification of A2 and limits to the cluster's velocity dispersion and core radius

Since not necessarily the whole source of cB58 has to be lensed into the gravitational arc cB58, and the magnification near critical lines is very model dependent, the magnitude of the unlensed source of cB58 can be obtained most accurately from the counterimage A2.

The most pessimistic statement concerning the magnification of A2 is obtained by considering the so-called mass-sheet degeneracy (e.g. Schneider & Seitz 1995) which states that all dimensionless observables (source separation and flux ratios of multiple images) are invariant under a transformation of the deflection potential according to

$$\psi_{\text{tot}}(x, y) \rightarrow \lambda\psi_{\text{tot}}(x, y) + (1 - \lambda)(x^2 + y^2)/2; \quad (20)$$

in other words, a potential can not be disentangled from a rescaled deflection potential (and thus a rescaled surface mass density and shear) and the addition of a constant mass sheet with $\kappa_0 = 1 - \lambda$; the constant λ is limited by the fact the the total surface mass density must not be negative.

From the ground based data of Gioia & Luppino (1994) we infer that the cluster is optically poor and confined to a small region; there is no hint that it is embedded in a larger scale structure which could provide the unconstrained mass sheet. Thus the ignorance about the mass-sheet degeneracy will add only a small uncertainty for the magnification of A2 relative to the unlensed source.

The unconstrained core radius of the cluster, however, can mimic the mass sheet degeneracy locally: increasing the velocity dispersion and the core radius of the cluster is similar to rescaling the potential and adding a constant surface mass density, as long as only a few positions (that of the multiple images) are considered and these positions are not spread enough in radius. If only the A and W system are taken into account for the model fit, a large cluster velocity dispersion can not be excluded, since then one can increase the core radius to suppress the central mass peak; for a velocity dispersion of $\sigma_{c1} = 840$ km/s one obtains a best fit core radius of about $20''$ and $\sigma_{cD} = 278$ km/s with a fit quality of $\Delta_W^2 \approx 300$ and $\Delta_A^2 = 2$. The magnification of A2 is then approximately 7. Even if one ignores the B and C system, a model demanding such a large core radius seems to be unplausible. On the other hand, if one uses only the positions A11, A12, A2 and W1, W2, WC and W3, the limits for σ_{c1} , $\epsilon_{c1, cD}$ as in the models before, and does not restrict the velocity dispersion of the cluster, a low value of its velocity dispersion and core radius is favored (the corresponding best fit values are summarized as MIVa in Table 2). The magnification of A2 agrees with that obtained for earlier models in Table 3.

Including the positions of the B-system must constrain the maximum velocity dispersion strongest. For a conservative estimate we ignore that B3 is most likely the third image to B1 and B2. In this case, an increase of the lensing strength for B1 and B2 for large velocity dispersions can be avoided by shifting them to lower redshift. Without a lower limit for the velocity dispersion of the cD, i.e. allowing for a redistribution of mass from the cD to the cluster and with restrictions for the remaining parameters as for model MIIa, we obtain a maximal acceptable velocity dispersion of the cluster of $\sigma_{c1} = 670$ km/s, with a core radius of $\approx 11''.2$ and a cD velocity dispersion of 250.8 km/s. The relative lensing strength of B then has to be $d_B \approx 0.9$, corresponding to a redshift of 1.7 in an Einstein-de Sitter universe. For this maximal velocity dispersion the magnification of A2 is equal to $\mu_{A2} = 3.4$. If B3 is the counterimage of B1 and B2, the maximal acceptable velocity dispersion has to be as low as 600–610 km/s to obtain a marginal fit with $\Delta_B^2 \leq 550$. Note that MIIb can not be considered as a good fit for B1, B2 and B3 and that in this case the sum in Table 3 includes only the positions of B1 and B2. For a cluster velocity dispersion of 600 km/s the velocity dispersion of the cD and the core radius become 257.8 km/s and $8''.8$. The magnification of A2 equals 2.56 in this case.

These investigations show that in fact the magnification of A2 is limited by $2.0 \lesssim \mu_{A2} \lesssim 3.4$ if B1, B2 are considered and even more ($2.0 \lesssim \mu_{A2} \lesssim 2.9^\ddagger$) if B3 is the third image

\ddagger These limits were not derived from a rigorous investigation, but contain all magnifications for A2 predicted by models which include B3 in their fit.

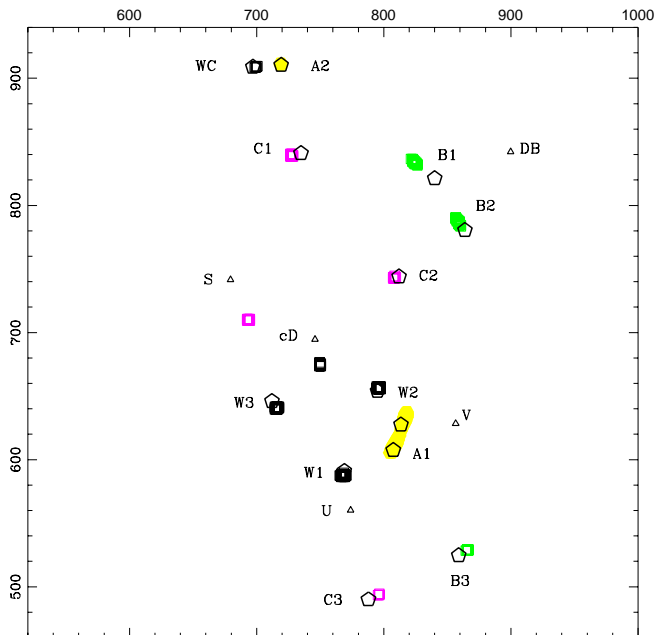


Figure 13. For model MIVa we used only the positions of the A and W-system to constrain the parameters describing the cD-galaxy and the cluster. The allowed range of parameters was limited by $\epsilon_{cD} \leq 0.2$, $\epsilon_{cl} \leq 0.25$ and $246 \text{ km/s} \leq \sigma_{cl} \leq 306 \text{ km/s}$. The cluster velocity dispersion was not limited. The multiple image positions for the C and B-system are predicted under the assumption $\sigma_{DB} = 84 \text{ km/s}$, $d_B = 1.02$ and $d_C = 1.035$.

of B1 and B2. Concerning the possible velocity dispersions of the cluster, the best fit parameters for the models MIa and MIb are almost as different as they can be to allow a good fit. We have tested this by giving different weights to different multiple image systems, by considering B1/B2/B3 instead of C1/C2/C3, by demanding that the ellipticity and orientation of the cD-potential equals that inferred from the light, by taking into account the galaxies V and S as possible deflectors etc. From this we infer limits of $540 \text{ km/s} \leq \sigma_{cl} \leq 670 \text{ km/s}$, $5''.5 \leq \theta_{cl} \leq 11''$ and $6^\circ \leq \phi_{cl} \leq 14^\circ$. Of course, these limits weaken, if one uses only the positions of the A or W system for the fit.

5.5 Alignment of cD-light, cD-potential and the cluster potential

In the models MI-IV the ellipticity and orientation of the cD potential were treated as free parameters. The best values for the ellipticity and orientation for those models are spread between $0 - 0.2$ and $\approx 11^\circ - 19^\circ$. This does not imply that the ellipticity and major axis of the cD potential is inconsistent with the values inferred from the light using Fig. 2 and the relation $\hat{\epsilon}_{cl} = 3\epsilon_{cl}$. Since lensing is only sensitive to the combined potential of the cD and the cluster, the orientation and ellipticity of the *individual* potentials are undetermined within some range (see Table 2). To demonstrate the consistency of the cD potential with the light distribution of the

cD we kept the cD parameters $\epsilon_{cD} = 0.06$ and $\phi_{cD} = 10^\circ$ fixed, varied those describing the cluster, the velocity dispersion of the cD ($246 \text{ km/s} \leq \sigma_{cD} \leq 306 \text{ km/s}$) and of DB ($70 \leq \sigma_{DB} \leq 100 \text{ km/s}$), and the redshifts of the W, C and B system. We used the positions of the A, W, B and C-system for the fit. With the exception of the B-positions the best fit model (MIVa) recovers the multiple image positions very well. When $\epsilon_{cD} = 0.11$ is assumed (model MIVb) the fit quality reduces. For MIVa&b the major axes of the potentials of the cD and the cluster are almost parallel. As a consequence, the fit quality stays comparable to the models MIVa&b, if one requires that the cD potential is strictly parallel to that of the cluster: we obtain $\phi_{cD} \equiv \phi_{cl} \approx 12^\circ$ (see model MIVc in Table 2). For the models MIVa&b the weights $w(i_k)$ in equation (14) were equal for all positions used for the fit. Since the multiple image positions are concentrated in the cluster core (W1,W2,W3,A11,A12) the mass profile is constrained most strongly there, and these observables are reproduced with the largest accuracy. Giving a weight of 2-3 to the positions of the C-system (B-system) and fitting the parameters in analogy to MIVc, the accuracy for the prediction of the C and B (B and C) system increases. This adds further weight to the hypothesis that both the C- and B-system are triple image systems. With the large weight to the outer multiple images, the orientation of the major axis of the cluster and cD potential decreases to 10 and 9 degrees. This tilt of the major axis of the potential is also seen in the light of the halo of the cD galaxy: for $\theta \leq 5''$ (A and W system) the position angle equals about 10° and drops to $\leq 8^\circ$ in that region where the images C and B occur ($\theta \leq 7''.5$).

We conclude, that the cD and the cluster are aligned and have a major axis position angle of about 10° , that the ellipticity of the combined potential increases and the position angle of the major axis changes in the outer parts of the cluster. The orientation of the major axis of the optical light and the dark mass thus agrees with that of the X-ray light found by Hamana et al. (1997).

6 THE MAGNIFICATION OF THE ARC

Up to now only two spots (A11 and A12) of the arc were used for the lens modelling, and they were treated as positions of multiple images. To make more use of the two-dimensional light distribution of the arc for the lens modelling, we consider only (CCD)-pixels where the counts exceed a rate of 5.5 and subdivide each pixel into two triangles (see Schneider, Ehlers & Falco 1992, page 300). For each model \vec{p} , all triangles of the arc are mapped into the source plane. Using a ≈ 50 times denser grid than in the lens plane, we identify for every triangle in the image plane all grid points in the source plane which lie within the corresponding triangle in the source plane. For a perfect model, each grid point in the source plane is contained either in no or in two triangles. In the second case one of these triangles has positive parity with respect to its corresponding triangle in the image plane (which is outside the critical line), and the other is mapped with negative parity onto the image plane (and the corresponding triangle is inside the critical line). Within the accuracy given by the finite spatial resolution of the CCD pixels, the surface brightness of such triangles should

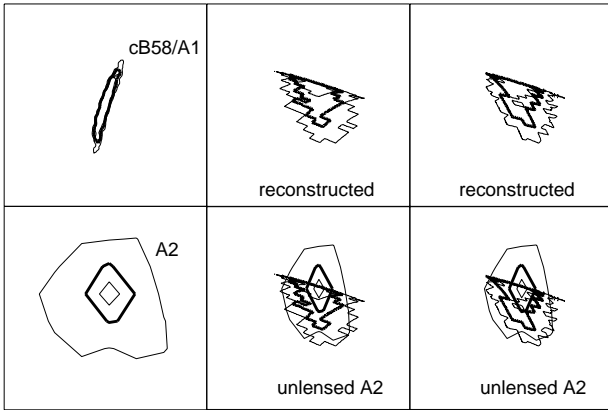


Figure 14. In all six panels we plot surface brightness contours of 5.5, 10 (thick contour) and 15 counts per pixel. The upper left panel has a side length of $5''$ and shows the surface brightness distribution of cB58. The remaining squares are $0''.35$ on a side. The upper middle and upper right panels show the reconstructed source (model MVIa) using the negative parity part and positive parity part of the arc, respectively. In the lower left panel the contours of the counterimage A2 can be seen. Using the surface density and shear at the position of A2 we ‘unlens’ the shape of A2 and obtain the squeezed contours in the lower middle and right panels. On top of that the corresponding contours of the reconstructed source of the arc are overlaid.

also agree. Gridpoints in the source plane which are singly imaged only reflect an imperfect model (and observational errors). To obtain a model which predicts the correct shape of the arc, we thus add a term proportional to

$$\eta := \frac{N_s - N_d}{N_s + N_d} \quad (21)$$

to (14), where N_s and N_d are the number of gridpoints in the source plane which are singly and doubly imaged, respectively. Note that adding a term proportional to N_s or $-N_d$ instead of (21) would introduce a bias towards high and low magnification of the arc. The value of (21) is independent of the magnification of the arc and equals (+1) and (-1) for a bad and for an optimal model. The best fit parameters are obtained in two steps: first the positions of the multiple images are used for the model fit and then the arc-shape constraint (21) is added in (14) and the minimization is continued. Whereas we generally use three positions (A11,A12,A2) to fix the arc and its counterimage, we consider only A11/A2 or A12/A2 when the shape is taken into account. This guarantees on the one hand that the global properties of the lens are changed only slightly and in particular that the counterimage stays at the same position; on the other hand, this allows changes in the mass distribution to turn the arc into the correct direction. In section 5 we showed that a good fit for the multiple image systems can be obtained by combining the deflection potential of the cluster and the cD galaxy. This is not the case for the arc shape: we can not obtain a good fit for the arc shape *and* the position of the W and A-system at the same time, because the arc demands a lot of shear parallel to its major axis. A possible

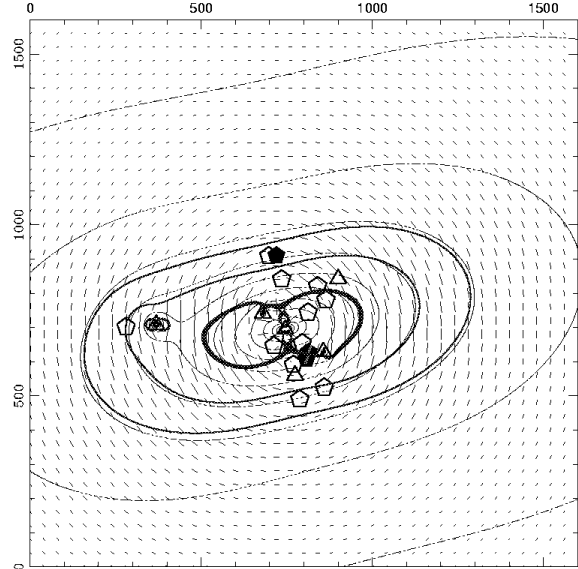


Figure 15. Shear field (vectors), surface density contours (dotted lines) and magnification contours (solid lines) for sources at redshift 2.7 according to the model MVIa. The surface density contours start at $\kappa = 0.1$ and are spaced by 0.1. Filled (empty) pentagons denote the positions of A11/A12/A2 (and the remaining multiply imaged galaxies). Other galaxies like the cD, the spiral, the elliptical E and the perturbers DB and V are added as empty triangles. The three thick contours are that of magnification 2, 3 and ‘infinity’, and thus the central thick contours denote the critical lines for a galaxy at redshift 2.7.

reason for the insufficient fit can be inferred from Fig.1&3: the arc is not entirely straight but curved, and the center of curvature points into the opposite direction that one expects if it is caused by the cD and the cluster. A possible cause of this curvature is a perturbation of the light deflection by the galaxy V on the right side of cB58: The galaxy V has the same blue color but a much smaller surface brightness than cB58. Thus it could be a blue, low surface brightness galaxy at low redshift or a ‘normal’ field galaxy at $z > 1$. We consider the first alternative as unlikely due to the small number density of those galaxies. If the redshift of V is ≥ 2 , then it lies close to, or on the critical curve of the lens corresponding to the redshift of V. The ‘close’ case can be ruled out because there is no ‘second’ image on the opposite side of the critical line with comparable brightness. The fact that V has a double core on the opposite sides of the $z \approx 2.7$ critical curve would favor the ‘on the critical line’ case. However, in that case a much more elongated object similar to cB58 would be expected and a counterimage on the right side A2 should be observable. The object 3.4 arcsec to the right of A2 is too far away and has too much of a red color to be an option. We conclude that the galaxy V is at redshift larger than one, but small enough to avoid being multiply imaged. In this case a two lens-screen situation arises, where the light of cB58 is distorted by the galaxy V before it is deflected by the cluster. Since we do not know the redshift of V we treat the light deflection as if it takes place at the redshift of the

cluster and model V as a singular isothermal sphere. The best fit velocity dispersion σ_V can then not easily be related to the depth of its potential, but describes only the ‘effective’ lensing strength of this galaxy. A two-screen model will only be useful once the redshift of V is known. Most generally, the velocity dispersion σ_V can be considered as a one-parameter correction for the effective shear and surface mass density at the arc.

For completeness we now also take into account the light deflection caused by the spiral S. This is done to show that the additional light deflection of the spiral does not change our preceding conclusions, i.e. that the multiple images positions are in agreement with the expectations from optical and X-ray light, and the dynamical properties of the cluster galaxies. Since none of the multiple images is close to the spiral, it adds only a small perturbation to their total deflection. Irrespective of its exact redshift ($z_S \approx 0.3$) we can therefore approximately describe its light deflection as taking place at the redshift of the cluster. We assume that the depth of its potential does not exceed 180km/s, which corresponds to the 3-dimensional velocity dispersion of a $1.8L_*$ -galaxy.

Fig. 14 shows the reconstructed sources for the arc cB58. It was obtained using the arc shape (as observed), and the A, B, C and W system with a low weight for the B-positions. The value of η defined in (21) equals -0.62 , and the remaining numbers characterizing the fit quality for the positions are shown in table 3 (model MVIa). The area of the arc in the source plane equals $3.61 - 4.46$ (dithered) pixels, where the range is obtained from either considering only the doubly imaged source pixels or all pixels in the source plane. This size is in agreement with that of the counterimage A2 (16 pixels) if one takes into account that A2 is magnified by a factor of 2.4 and if about half of the total source is lensed into the gravitational arc cB58 (as is indicated in Fig. 14 as well). From the size ratios of the arc source ($3.61 - 4.46$ pixels) and the non-deconvolved arc (213 pixels) we obtain a magnification factor of $\mu_{\text{arc}} \approx 47.8 - 59.0$ within the contour of 5.5 counts per pixel. In Fig. 14 we have also unlensed the shape of A2 using the predicted surface density and shear of the model MVIa at the position A2. On the surface brightness contours of the unlensed object A2 we have overlaid those of the reconstructed source of cB58. The contours of 5.5 counts per pixel agrees very well, although only the shape and not the flux distribution of the arc was used for the model fit. The contour at 10 counts per pixel is a bit larger for the reconstructed arc source than for the unlensed counterimage. These differences can be attributed to the finite pixel size in the image of A2. Fitting the shape of the arc adds only a local constraint to the model and does not break the velocity dispersion-core radius degeneracy discussed before. Thus the total magnification of the arc will also increase if the velocity dispersion and core radius are increased. The corresponding magnification of the arc can however be estimated from the magnification of the counterimage: using that the sizes of the arc and A2 are 213 and 16 pixels within the 5.5 counts per pixel contour, and that only a fraction $f \approx 1/2$ of the total source is imaged into the arc cB58 one can roughly estimate the arc magnification to be $\mu_{\text{arc}} \approx 213/16 \mu_{\text{A2}}/f \approx 25 \mu_{\text{A2}}$.

In Fig. 15 the gravitational shear field, the surface mass density, and magnification contours are plotted for the

model MVIa. The shear field is a measure for the direction and ellipticity that a circular source obtains through the lens effect of the combined mass distribution at the same position. One can see that the shear field left to the elliptical E is parallel to the y -direction of the chip, and thus explains the large distortion of the arclet left of E (its magnification equals 3 for a redshift similar to cB58). The surface density contours start at $\kappa = 0.1$ and are separated by $\Delta\kappa = 0.1$. Independent of the details of the model the mean surface density in the chip-3 is $\langle\kappa\rangle \approx 0.2$. The thick contours are that of magnification 2, 3 and infinity (critical line for a source at $z = 2.7$).

7 WEAK LENSING ANALYSIS

We next consider the distortion of images of (presumably background) galaxies near the core of MS1512. With this analysis we do not aim at a weak lensing mass reconstruction as in the case of Cl0939+4713 (Seitz et al. 1996) – where the observations were deeper and the lens stronger – but at a consistency check of the weak lensing signal with the cluster parameters estimated from multiple images. We use the coadded V and R-data and consider only galaxies in the WFPC-fields which are within a distance of 80 to 850 pixels (i.e. within a distance of $42''.5$) from the center of light of the cD galaxy. The outer radius equals the maximum radius of a circular disc centered on the cD galaxy which is completely within the data region. A size cut of 50 (dithered) pixels is applied, and stars and objects with a SExtractor-flag larger than 16 are excluded. This excludes objects with incomplete or corrupted aperture or isophotal data.

The minimum flux of galaxies considered for the weak lensing analysis was set equal to that of the completeness limit of the numbercounts in the V+R-data. The bright cutoff was set 2.5 times this limiting flux. Comparing the number counts for these galaxies in the WFPC2 field with published results on the I-band counts (Smail et al. 1995), we estimate that the selected galaxies have I-band magnitudes of about $23.3 \lesssim m_I \lesssim 24.3$. According to the evaluation of the CFR-Survey (Lilly et al. 1995) the mean redshift of those galaxies is predicted to be of order one.

The shapes of the galaxies are estimated with the SExtractor software package (Bertin & Arnouts 1996). The width σ_χ of the ellipticity distribution of the remaining 33 (29 of them are within chip-3) galaxies is estimated and it is assumed (and checked) that this width is basically unaffected by lensing. The deflection potential of the cluster is described by (1), with the ellipticity, orientation and velocity dispersion as free parameters, and the core radius is assumed to be equal to 150 pixel. Let χ_i be the complex ellipticity as defined eg. in Schneider & Seitz (1995) of the i -th object, and $\langle\chi\rangle_i(\vec{p})$ the model dependent expectation value at the same position; further let $\sigma_{\chi t_i}(\vec{p})$ (for details on $t_i(\vec{p})$ see also Schneider & Seitz 1995) be the width of the ellipticity distribution expected at the position of the i -th object for lensing parameters \vec{p} ; we then minimize:

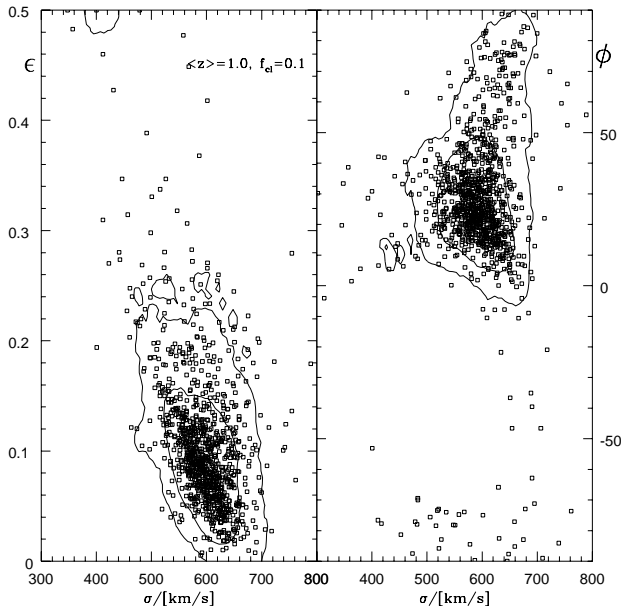


Figure 16. Best fit estimates for the clusters velocity dispersion, ellipticity and major axis position angle using 1000 bootstrapped realizations of galaxies with $24 \leq m_{V+R} \leq 25$ within 850 pixels distance to the cD galaxy. The contours approximately indicate that region in which 68 and 90 percent of the best-fit values are contained. The mean redshift of the galaxies and the contamination with cluster members were assumed to be $\langle z \rangle \approx 1.0$ and $f_{cl} = 0.1$

$$F := - \sum_{i=1}^{n_{gal}} \ln \left\{ (1 - f_{cl}) \frac{1}{t_i^2(\vec{p})} \exp \left[\frac{-|\chi_i - \langle \chi \rangle_i(\vec{p})|^2}{\sigma_\chi^2 t_i^2(\vec{p})} \right] + f_{cl} \exp \left[-\frac{|\chi_i|^2}{\sigma_\chi^2} \right] \right\} \quad (22)$$

with respect to \vec{p} ; for the contamination of the galaxy sample with cluster members (or foreground galaxies) we assume $f_{cl} = 0.1$. To parametrize the distance to the galaxies we assume in analogy to Eqs. (15)-(17) a relative lensing strength of $d = 0.72$ which corresponds to a mean redshift of $\langle z \rangle \approx 1$ in an Einstein-de Sitter universe. For 1000 bootstrapping realizations of the data catalog we determine the best fitting parameters for the velocity dispersion, the major axis position angle and the ellipticity of the clusters deflection potential. The result is shown in Fig. 16 where each point in the $\epsilon_{cl}-\sigma_{cl}$ and $\phi_{cl}-\sigma_{cl}$ plane corresponds to a best fit for one bootstrapped data catalog. We added contours in which approximately 90 and 68 percent of the best fit parameters are contained. According to Fig. 16 the $1-\sigma$ interval for the velocity dispersion and the major axis position angle equals $[520, 670]$ km/s and $[5^\circ, 50^\circ]$, with best fit values of about 600 km/s and 20° . We point out that the estimate for the velocity dispersion depends on the mean redshift assumed for the galaxies and on f_{cl} . If that former was equal to 0.8

instead of 1, the estimated velocities increase by 10 percent. Another uncertainty is the unknown core radius since the data field ($42''$ radius) is not very large compared with the core radius ($150 \text{ pix} = 7''.5$). If the core radius is allowed to vary between 120 and 200 pixels, the distribution of the points the $\epsilon-\sigma_{cl}$ -plane becomes broader, in particular towards larger velocity dispersions, since a larger core radius can be compensated by an increased velocity dispersion. But even in this case both the 68 and 90 percent upper confidence limits for the velocity dispersion are still below 800km/s. The assumption of a core radius of 150 pixels is, by the way, not unreasonable because it agrees with that found from the X-ray observations of this cluster (Hamana et al. 1997).

8 SUMMARY AND DISCUSSION

We have shown that the ‘protogalaxy’ cB58 owes its large apparent brightness to the lens effect caused by the cluster MS1512 and its cD galaxy. The symmetry in the surface brightness distribution reveals that cB58 is a gravitational fold arc; the large axis ratio is caused by the stretching of the source parallel to the major axis of the arc.

Three systems of multiply imaged galaxies are found. In the first case (W), a shrimp-like object is mapped into five images, of which four can be identified. The redshift of the W-system must be very similar to that of cB58. Measuring the flux ratios and colors of the galaxies of the W-system is difficult, because all objects are small, not much above the noise level, or their colors are affected by red light and absorption caused by the cD galaxy.

The second system (C) consists of three images which also have not well determined and slightly inconsistent colors. The three images of the system have the same head-tail morphology, their positions can most robustly be fitted for different parameters of the lens models, and the relative inclinations of their head-tail axes agrees with the predictions from lens models. For most models the source redshift is $z \approx 3.5$.

The third system (B) is also a triple system; two images are close to the tangential critical line and their magnification is affected by a nearby elliptical galaxy (DB) with an estimated velocity dispersion of $\sigma_{DB} = 84 \text{ km/s}$. The estimated redshift of the source is ≈ 3 . However, a precise prediction for the redshifts of the B and C-system is difficult, since the lensing strength increases only slowly with redshift (see Fig. 9) and thus a broad range of redshifts is formally possible. An upper limit of $z < 4$ for the B and C system is set by their detectability in the B-band observations of Gioia & Luppino (1994).

The lens system was modelled with a singular (non-singular), elliptical isothermal potential for the cD galaxy (for the cluster) and isothermal potentials for additional galaxies. Because the multiple images are not spread much in radius, a core radius-velocity dispersion degeneracy arises; if only the inner image systems (W and A) are considered, a cluster velocity dispersion of 840 km/s can not be excluded if a core radius as large as $\approx 20''$ is accepted. Without any restriction to the cluster velocity dispersion, lower values for σ_{cl} and ζ_{cl} are favored. Giving equal weight to all multiply imaged objects, the inner multiple image systems are fitted

better than the outer ones, because a high weight is given to the central mass profile. With an increased weight to the outer images, the outer positions can be fitted better, at the cost of the central images. This is expected since we have more observables (12 image positions = 24 observables) and up to 11 to 13 free parameters (4 for the cluster, 3 for the cD, one for DB, three for the redshifts of the W, C and B system, possibly also one for V and S) and one can not expect the true mass distribution to follow the model in every detail. Most likely, there is a change of the ellipticity and orientation of the cluster potential with radius as it is visible in the cD light and in the X-ray contours.

The best fit cluster velocity dispersions are of the order of 600km/s and thus are at the low end of the dynamical estimates of Carlberg et al. (1996a, b). However, the amplitude $\psi_0 \propto \sigma_{cl}^2$ determined by the lens modelling can be easily related to the ‘real’ dynamical velocity dispersion only in the spherical symmetric case where $\sigma_{cl} \equiv \sigma_{dyn}$ should hold. Under the two assumptions, the weak lensing analysis confirms a low velocity dispersion σ_{cl} of the cluster: The first is that the core radius of the cluster is approximately $7''.5$; this assumption is assisted by the X-ray results of Hamana et al. (1997) [$(6.9 \pm 1.4)''$ or $(7.5 \pm 1.5)''$, according to the two cases analyzed there] which normally do not overestimate the core radius of the dark mass profile. And secondly we have assumed – after comparing the number counts to that of the I-band and using the CFRS-results – that the mean redshift of the galaxies used for the weak lensing analysis is one. Since the cluster velocity dispersion is in agreement with the value of Carlberg et al. (1996 a&b), this is also the case for the total mass estimate and the mass to light ratio of the cluster: i) if we consider only the velocity dispersions $\sigma_{cl} \approx 600\text{km/s}$ and $\sigma_{dyn} = (690 \pm 100)\text{km/s}$ derived from lensing and peculiar velocities and ignore the asymmetry for the mass estimate within the virial radius, the lensing mass is 75% of the dynamical mass, but of course compatible to it within the error bars. ii) Including all galaxies considered for the light deflection, we obtain (for a Einstein-de Sitter cosmology) a mass within chip-3 of $\approx 8 * 10^{13} h_{50}^{-1} M_{\odot}$, which transfers to a mass of $1 * 10^{15} h_{50}^{-1} M_{\odot}$ within the virial radius of $1.803 h_{100}^{-1} \text{Mpc}$ (Carlberg et al. 1996b), if the combined mass profile of the cluster and its galaxies is isothermal out to the virial radius. The Carlberg et al. (1996a) value is $5.5 * 10^{14} h_{100}^{-1} M_{\odot}$ (for $\Omega = 0.2$) and this estimate decreases by about 10 percent if one uses $\Omega = 1$.

Hamana et al. (1997) suggested to use the measured quantities (in their case the X-ray temperature and the core radius of MS1512) to model the lensing of cB58 and to derive limits for the cosmological constant (for flat universes). Although velocity dispersion estimates would drop by $\approx 15\%$ for a flat $\Omega = 0.3$ universe relative to an Einstein-de Sitter universe, we do not consider this as a promising method, because the true mass distribution is only described approximately by two elliptical potentials, and the best fit value σ_{cl} can not straightforwardly be related to the measured σ_{dyn} . A comparison of the relative lensing strengths for the multiple images at different source redshifts will not improve this situation, although these estimates are less model dependent. The reason is that the lensing strength of a $z = 3.17$ source relative to that of cB58 equals 1.0250, 1.0217 and 1.0195 for an Einstein-de Sitter, a flat $\Omega = 0.3$ and a $\Omega = 0.3$

universe with vanishing cosmological constant, and thus the fractional differences are in the permille range.

Using imaging and spectroscopy under excellent seeing conditions could further improve the lens models: Deeper photometry in V and R or additional filters can show that B3 is the third image corresponding to B1 and B2. If the flux ratios of all the multiply imaged galaxies can be obtained more accurately, they can quantitatively be included into the lens modelling. We consider this as difficult since then a filter needs to be chosen where the absorption and emission of the cD are small, and where the blue galaxies C and W are bright enough. If the redshift of V (and not so important but much easier: the redshift of S) is determined, a two-screen model can be used. The uncertainty in the lensing strength of B and C (see Table 2) is much larger than the minimum uncertainty given by the unknown cosmological parameters. Therefore redshift measurements of the C and B-system can improve the constraint on the slope and thus the core radius of the potential.

One of the goals of our investigations was to show that cB58 is a fairly ‘normal’ high-redshift galaxy. This becomes most obvious when the counterimage A2 is considered and its magnification of $\mu_{A2} = 2 - 3.5$ is taken into account. Therefore, cB58 is 3.35-4 magnitudes brighter than its unlensed (total) source. If one shifts the data point for cB58 in the magnitude-redshift plane in Fig. 5 of Lowenthal et al. (1997) by that amount, one sees that the source of cB58 is a normal ‘ $z = 3$ -Steidel galaxy’ in the I-magnitude - redshift plane. This is also valid for the source size: the half-light radius of A2 is $0''.25 \pm 0''.05$ in the V and R band, which equals $3h_{50}^{-1}\text{kpc}$, $3.75h_{50}^{-1}\text{kpc}$ and $1.9h_{50}^{-1}\text{kpc}$ in a $q_0 = 0.05$, a Einstein-de Sitter, and a flat universe with $\Omega = 0.1$. The half-light angle agrees with that found by Steidel et al. (1996b) for galaxies of the same redshift. Including the minimum magnification $\mu_{A2} \gtrsim 2$ of A2 decreases the half-light radius by 30 percent, i.e. to $0''.18$ or $2.1h_{50}^{-1}\text{kpc}$ for $q_0 = 0.05$. Thus the unlensed source A agrees in R-magnitude, redshift and half light radius with the galaxy C2-05 in the HDF (Steidel et al. 1996b). To compare with absolute B-band luminosity of other high redshift galaxies (Lowenthal et al. 1997, Fig. 6) we avoid the uncertainties related to the k_V correction and simply consider the H band which is approximately equivalent to the rest B band at $z=2.72$. We then correct the $m_H = 19.82$ for extinction according to the $E(B - V) = 0.3$ given by Ellingson et al. (1996). The authors found that a 10 Myr old constant star formation model with this amount of extinction provides the best fit to the optical-IR data of the galaxy. Therefore, taking into account the uncertainties in the magnification factor and the extinction correction, the m_H implies a rest frame B absolute magnitude in the range $-25.43 \leq M_B \leq -24.05$ ($H_0 = 75 \text{ km}^{-1} \text{ sec}^{-1} \text{ Mpc}^{-1}$, $q_0=0.05$) quite close to the $M_B \simeq -24$ in Lowenthal et al. (1997). An even better agreement is obtained if the lower value $E(B - V) = 0.1$ adopted by Lowenthal et al. (1997) is used.

The enormous size and flux of cB58 can be attributed to the gravitational lens effect. This is of course not the case for the surface brightness, which is conserved by lensing. Since the surface brightness stays high all over cB58 and it is fairly structureless (despite of the spots in Fig. 3, which are not visible from ground) this was interpreted as an indication for a simultaneous and high star formation spread

over the entire galaxy, and therefore cB58 was denoted a primeval galaxy. The reconstruction of the source of the arc shows that only a part of the source is lensed into cB58, and that those regions with highest surface brightness experience the largest magnification. The light distribution of cB58 is a ‘zoom’ into the central part of its source where the star formation rate is high. The comparison of the spectral properties (line width and ratios) of cB58 and its counterimage will therefore give limits on the inhomogeneity of the star formation in the source of cB58 with unprecedented spatial resolution.

It seems surprising that a ‘weak’ cluster with a velocity dispersion of $\sigma \approx 600\text{km/s}$ can act as a strong lens, and that not only one but four multiple image systems are found. This can be attributed to the high surface density of $z > 2$ galaxies (Lowenthal et al. 1997) and the increased lensing strength for these sources, compared to $z \approx 1$ galaxies. With the sources A, B, C, W and the arclet lying $12''$ N-NE of the cD (which is similar in color and surface brightness to B1/B2) we have at least 5 candidates with a redshift larger than 2 (or 2.5) within a radius of 15 arcseconds around the cluster center, corresponding to a large number density of ≈ 25 galaxies per square arcminute. This number density increases when one takes into account that these sources originate from a much smaller area in the source plane and that the slope of the logarithmic number counts at those redshifts is probably not steeper than 0.4. Comparison to predicted and observed high redshift number counts are difficult due to the individual magnification of the galaxies and since these investigations use galaxies with a flux limit in the I or ‘I+V’-band. The large number of high redshift galaxies can also be caused by statistical fluctuations or by a group of galaxies at $z = 2.7$, since we can not exclude that the sources of the W and B-system are at the same redshift as cB58. Our investigation show as well as that of Franx et al. (1997) and Trager et al. (1997), that the analysis of galaxies lensed by foreground clusters provides a highly successful method to find high-redshift galaxies.

Finally, we have shown that a cluster with a velocity dispersion as low as $\sigma \approx 600\text{km/s}$ is not only detectable by weak lensing methods, but its velocity dispersion is still measurable within an accuracy of 150km/s at a one sigma level. This confirms the claim (Schneider 1996) that even less massive dark matter halos can be detected at a statistically significant level under the same observing conditions as here and that halos of the same depth can be detected in shallower observations with a larger point spread function.

ACKNOWLEDGMENTS

We thank J.-P. Kneib and Y. Mellier for discussion on the multiple image systems. We are grateful to G. Luppino for providing us with the ground-based data on MS1512 in the R- and B-band and to R. Carlberg for providing us with the positions of redshift-confirmed cluster members. We also thank P. Schneider for encouraging discussion and valuable suggestions on the manuscript. This work was supported by the ‘‘Sonderforschungsbereich 375-95 für Astro-Teilchenphysik’’ der Deutschen Forschungsgemeinschaft.

REFERENCES

- Asada, H., 1996, astro-ph/9611110
 Bender, R., Saglia, R.P., Ziegler, B., Belloni, P., Greggio, L., Hopp, U., Bruzual, G., 1997, submitted to ApJL
 Bender, R., Möllenhoff, C., 1987, A&A, 177, 71
 Bertin, E., Arnouts, S., 1996, A&AS, 117, 393
 Bruzual, G.A., Charlot, S., 1993, ApJ, 405, 538
 Bruzual, G.A., Charlot, S., 1997, submitted to ApJ
 Carlberg, R., Yee, H.K.C., Ellingson, E., Abraham, R., Gravel, P., Morris, S., Pritchet, C.J., 1996a, ApJ, 462, 32
 Carlberg, R., Yee, H.K.C., Ellingson, E., Morris, S., Abraham, R., Gravel, P., Hartwick, F.D.A., Hesser, J.E., Hutchings, J.B., Oke, J.B., Pritchet, C.J., Smecker-Hane, T., 1996b, ApJ, 462, 32
 Dressler, A., Faber, S.M., Burstein, D., Davies, R.L., Lynden-Bell, D., Terlevich, R.J., Wegner, G., 1987, ApJ, 313, L37
 Ebbels, T.M.D., Le Borgne, J.F., Pello, R., Ellis, R.S., Kneib, J.-P., Smail, I., Sanahuja, B., 1996, MNRAS, 281L, 75
 Ellingson, E., Yee, H.K.C., Bechtold, J., Elston, R., 1997, ApJ, 466, L71
 Franx, M., Illingworth, G.D., Kelson, D.D., van Dokkum, P.G., Tran, K-V, 1997, preprint
 Frayer, D.T., Papadopoulos, P.P., Bechthold, J., Seaquist, E.R., Yee, H.K.C., 1997, ApJ, 113, 562
 Fukugita, M., Futamase, T., Kasai, M., Turner, E.L., 1992, ApJ, 393, 3
 Gioia, I.M., Luppino, G.A., 1994, ApJS, 94, 583.
 Hamana, T., Hattori, M., Ebeling, H., Henry, J.P., Futamase, T., Shioya, Y., 1997, astro-ph/9703136
 Holtzman, J.A., Burrows, C.J., Casertano, S., Hester, J.J., Trauger, J.T., Watson, A.M., Worthey, G., 1995, PASP, 107, 1065
 Kneib, J.-P., Mellier, Y., Fort, B., Mathez, G., 1993, A&A, 273, 367
 Kneib, J.-P., Mathez, G., Fort, B., Mellier, Y., Soucail, G., Longaretti, P.-Y., 1994, A&A, 286, 701
 Kneib, J.-P., Ellis, R.S., Smail, I., Couch, W.J., Sharples, R.M., 1996, ApJ, 471, 643
 Lilly, S.J., Tresse, L., Hammer, F., Crampton, D., Le Fevre, O., 1995, ApJ, 455, 108
 Lowenthal, J.D., Koo, D.C., Guzman, R., Gallego, J., Phillips, A.C., Faber, S.M., Vogt, N.P., Illingworth, G.D., Gronwall, C., 1997, ApJ, 481, L673
 Lucy, L., 1974, AJ, 79, 745
 Mellier, Y., Soucail, G., Fort, B., Le-Borgne, J.-F., Pello, R., 1990, in *Gravitational Lensing*, Mellier, Y., Fort, B., Soucail, G. (eds.), Springer
 Mellier, Y., Fort, B., Kneib, J.-P., 1993, ApJ, 407, 33
 Press, W.H., Teukolsky, S.A., Vetterling, W.T. & Flannery, B.P., 1992, *Numerical Recipes*, Cambridge University Press
 Saglia, R.P., Bender, R., Ziegler, B., Belloni, P., Greggio, L., Hopp, U., Bruzual, G., 1997, in preparation
 Schneider, P., Ehlers, J., Falco, E., 1992, *Gravitational Lenses*, Springer, Heidelberg
 Schneider, P., Seitz, C., 1995, A&A, 294, 411
 Schneider, P., 1996, A&A, 283, 837
 Seitz, C., Kneib, J.P., Schneider, P., Seitz, S., 1996 A&A, 314, 707
 Smail, I., Hogg, D.W., Yan, L. & Cohen, J.G., 1995, ApJ, 449, L105
 Steidel, C.C., Giavalisco, M., Pettini, M., Dickinson, M., Adelberger, K.L., 1996a, ApJ, 462, 17
 Steidel, C.C., Giavalisco, M., M., Dickinson, M., Adelberger, K.L., 1996b, AJ, 112, 352
 Trager, S.C., Faber, S.M., Dressler, A., Oemler, A.Jr., 1997, astro-ph/9703062
 Williams, L. L. R., Lewis, G.F., 1997, MNRAS, 281, L35 (WL)

Yee, H. K. C., Ellingson, E., Bechtold, J., Carlberg, R. G., Cuil-
landre, J.-C., 1996, *AJ*, 111, 1883 (Y96)

Ziegler, B., Bender, R., 1997, *MNRAS*, in press (astro-
ph/9704280)

Ziegler, B., 1996, PhD Thesis, University Heidelberg

Ziegler, B., 1997, in preparation

This figure "CB58_fig.gif" is available in "gif" format from:

<http://arxiv.org/ps/astro-ph/9706023v1>